Longitudinal and transversal resonant tunneling of interacting bosons in a two-dimensional Josephson junction: Mean-field and many-body dynamics

Anal Bhowmik[1,2,*] and Ofir E. Alon[1,2]

[1] *Department of Mathematics, University of Haifa, Haifa 3498838, Israel*

[2] *Haifa Research Center for Theoretical Physics and Astrophysics, University of Haifa, Haifa 3498838, Israel*

(Dated: October 13, 2021)

We unravel the out-of-equilibrium quantum dynamics of a few interacting bosonic clouds in a two-dimensional asymmetric double-well potential at the resonant tunneling scenario. At the single-particle level of resonant tunneling, particles tunnel under the barrier from, typically, the ground-state in the left well to an excited state in the right well, i.e., states of different shapes and properties are coupled when their one-particle energies coincide. In two spatial dimensions, two types of resonant tunneling processes are possible, to which we refer to as longitudinal and transversal resonant tunneling. Longitudinal resonant tunneling implies that the state in the right well is longitudinally-excited with respect to the state in the left well, whereas transversal resonant tunneling implies that the former is transversely-excited with respect to the latter. We show that interaction between bosons makes resonant tunneling phenomena in two spatial dimensions profoundly rich, and analyze these phenomena in terms of the loss of coherence of the junction and development of fragmentation, and coupling between transverse and longitudinal degrees-of-freedom and excitations. To this end, a detailed analysis of the tunneling dynamics is performed by exploring the time evolution of a few physical quantities, namely, the survival probability, occupation numbers of the reduced one-particle density matrix, and the many-particle position, momentum, and angular-momentum variances. To accurately calculate these physical quantities from the time-dependent many-boson wavefunction, we apply a well-established many-body method, the multiconfigurational time-dependent Hartree for bosons (MCTDHB), which incorporates quantum correlations exhaustively. By comparing the survival probabilities and variances at the mean-field and many-body levels of theory and investigating the development of fragmentation, we identify the detailed mechanisms of many-body longitudinal and transversal resonant tunneling in two dimensional asymmetric double-wells. In particular, we find that the position and momentum variances along the transversal direction are almost negligible at the longitudinal resonant tunneling, whereas they are substantial at the transversal resonant tunneling which is caused by the combination of the density and breathing mode oscillations. We show that the width of the interparticle interaction potential does not affect the qualitative physics of resonant tunneling dynamics, both at the mean-field and many-body levels.

In general, we characterize the impact of the transversal and longitudinal degrees-of-freedom in the many-boson tunneling dynamics at the resonant tunneling scenarios.

* abhowmik@campus.haifa.ac.il

I. INTRODUCTION

Tunneling is a purely quantum mechanical phenomenon which takes place in classically-forbidden region, originally intended to account for α-decay, fusion, and fission in nuclear physics [1, 2]. Apart from nuclear physics, tunneling occurs naturally in photoassociation and photodissociation processes, and in solid-state structures [3–7]. Ultracold quantum gasses have been the subject of research to simulate solid-state systems [8–13]. In the context of the study of tunneling dynamics of ultracold atoms, a double-well potential with static barrier is a standard example. Most of the tunneling phenomena were investigated with ultracold atoms in one dimension, either in a double-well potential or in periodic optical lattices, and focused on the atomic motion in the lowest band, i.e., particularly with the ground state [14–19]. Moreover, it was shown in a double-well potential that the inclusion of higher single-particle levels is fundamentally important for correlations [20, 21]. Josephson-like dynamics of a Bose-Einstein condensate of rubidium atoms was investigated in the second Bloch band of an optical square lattice [22]. Unconventional orbital superfluidity in the P- and F-bands of a bipartite optical square lattice was achieved in [23, 24]. Recently, we explored the tunneling dynamics of ultracold bosons in a symmetric double-well potential where the atomic motion lies in the ground as well as excited bands [25].

The interband quantum tunneling of ultracold atoms between the ground and excited bands can occur by breaking the symmetry of the two wells of a symmetric double-well potential, say, by generating an asymmetric double-well potential. This asymmetric double-well potential can be understood as a unit cell of a tilted optical lattice [26–29]. Also, an external electromagnetic field can induce interband transitions as demonstrated in the spectroscopy of Wannier-Stark levels [30]. Here, we are interested in the interband quantum tunneling in an asymmetric double-well potential, typically describes in the tilted optical lattice. Per definition, the interband tunneling in an asymmetric double-well potential occurs when the energy of the ground state on one side of the double-well coincides with the energy of an excited state on the other side. This leads to tunneling between those states which is resonantly enhanced by the energy matching, usually referred to as resonantly enhanced tunneling [31, 32].

Resonantly enhanced tunneling phenomenon has been observed in various fields of research, such as in a nonlinear effect in a Mott insulator by creating a particle-hole excitation [33], in the presence of many-body coherences [34], in waveguide arrays [35], in an optical lattice with an external magnetic field producing a Zeeman splitting of the energy levels [36], in the two-terminal current-voltage characteristics of a finite superlattice [37], in solid states systems such as

superlattice [5, 38], and in accelerated optical lattice potentials [27, 28].

Hitherto, resonantly enhanced tunneling is studied when the resonant condition of energy matching of the two wells is along the direction of the barrier [31, 32, 39]. We name it longitudinal resonant tunneling. In Ref. [32], the condensates were prepared in a one-dimensional optical lattice with an additional Stark force and determined the tunneling rate by the Landau-Zener formula [40–44]. Zenesini *et al.* experimentally investigated the impact of atom-atom interactions on the resonantly enhanced tunneling process and presented a complementary theoretical description of Landau-Zener tunneling for ultracold atoms in periodic potentials [31]. The out-of-equilibrium quantum mean-field and many-body dynamics of interacting bosons were recently explored in a one-dimensional asymmetric double-well potential [39] using the multi-configurational time-dependent Hartree for bosons (MCTDHB) method [45–47]. Precisely, the interacting bosons were prepared in the ground state of the left well (harmonic potential) and the mechanism of the tunneling process in the resulting double-well was studied by analyzing the time-evolution of the survival probability, depletion and fragmentation, and the many-particle position and momentum variances [39].

Resonant tunneling in a two-dimensional (2D) double-well setup brings interesting new questions, especially on the role of transverse excitations. Also, in 2D there can be a resonant tunneling phenomenon which does not exist in one-dimension, namely, transversal resonant tunneling when the energy-matching condition of the two wells of an asymmetric double-well is satisfied along the transverse direction of the barrier. In this work, we focus on the longitudinal and transversal resonant tunneling for the initial bosonic structures of the ground and excited states in a 2D asymmetric double-well potential. Here the bosons are loaded in the left well of the double-well potential and the barrier is formed along the x-direction. In order to investigate the tunneling dynamics in the longitudinal resonant scenario, we consider two different structures of bosonic clouds, i.e., the ground and transversely excited (y-excited) states. Although, the ground state has a one-dimensional analog, to create a transversely excited state, one requires at least a 2D geometry [25]. Therefore, to investigate the effect of the longitudinal resonant tunneling on the very basic state which includes transverse excitations is of fundamental interest. Moreover, we investigate the impact of the transverse direction on the tunneling dynamics of the ground state at the longitudinal resonant tunneling condition. In the transversal resonant scenario, the bosonic structures are assumed to be the ground and longitudinally excited (x-excited) states. These two states have one-dimensional analogs but the transversal resonant tunneling does exist only in a 2D geometry. Therefore, the role of longitudinal excitations in transversal resonant tunneling can be examined. In order to accurately explore the out-of-equilibrium tunneling dynamics for both

resonant tunneling scenarios, we solve the underlying time-dependent many-boson Schrödinger equation using the MCTDHB method [46, 47]. We solve the quantum dynamics of all the bosonic clouds at the mean-field and many-body levels.

Tunneling dynamics for all the bosonic structures are analyzed by the time evolution of various physical quantities, namely, the survival probability, loss of coherence, depletion and fragmentation, and the many-particle position, momentum, and angular-momentum variances. Even when the bosons are fully condensed, the variance is a sensitive probe of correlations [48]. Therefore, to display the effects of the quantum correlations on the variances of different operators, we compare the mean-field and many-body variances in addition to the corresponding comparison of the survival probabilities. We notice that the rate of growth of the quantum correlations depends on the shape of the bosonic clouds, presence of transverse excitations in the system, and the resonant tunneling condition. The interconnection between the density oscillations and the variances are discussed both at the longitudinal and transversal resonant tunneling scenarios. We show that correlations have different consequences on the various quantities discussed in this work. In general, we ask how the transverse degrees-of-freedom, perpendicular to the junction, can influence the time evolution of various physical quantities in a 2D asymmetric double-well potential at the resonant tunneling scenario. We find that the time evolutions of the variances behave completely differently in the longitudinal and transversal resonant tunneling conditions.

II. THEORETICAL FRAMEWORK

The dynamics of N interacting bosons in a two-dimensional trap can be described by the time-dependent many-body Shrödinger equation,

$$\hat{H}\Psi = i\frac{\partial \Psi}{\partial t}, \qquad \hat{H}(\mathbf{r}_1.\mathbf{r}_2, ..., \mathbf{r}_N) = \sum_{j=1}^{N}[\hat{T}(\mathbf{r}_j) + \hat{V}(\mathbf{r}_j)] + \sum_{j<k}\hat{W}(\mathbf{r}_j - \mathbf{r}_k), \tag{2.1}$$

where $\hat{T}(\mathbf{r})$ and $\hat{V}(\mathbf{r})$ represent the kinetic and potential energy terms, respectively. The interaction between the bosons is repulsive and considered as a Gaussian function [49] $W(\mathbf{r}_1 - \mathbf{r}_1) = \lambda_0 \frac{e^{-(\mathbf{r}_1-\mathbf{r}_2)^2/2\sigma^2}}{2\pi\sigma^2}$ with $\sigma = 0.25\sqrt{\pi}$. In Appendix B, we investigate the role of the width of the interparticle interaction potential and demonstrate explicitly that the mean-field and many-body physics found in this work do qualitatively not depend on this width. λ_0 is the interaction strength and Λ the interaction parameter. $\Lambda = \lambda_0(N-1)$ where N is the number of bosons. Note that the model inter-bosons interaction does not have any qualitative impact on the physics described here.

In order to solve Eq. 2.1 in-principle numerically exactly, we use the multi-configurational time-dependent Hartree for bosons (MCTDHB) method [18, 19, 39, 45, 46, 48, 50–68]. MCTDHB incorporates a variational optimal ansatz which is generated by distributing the N bosons over M time-dependent orbitals. The MCTDHB wavefunction is described as [46]

$$|\Psi(t)\rangle = \sum_{\{\mathbf{n}\}} C_{\mathbf{n}}(t)|\mathbf{n};t\rangle, \tag{2.2}$$

where $C_n(t)$ is the expansion coefficients and $|\mathbf{n};t\rangle = |n_1, n_2, ..., n_M; t\rangle$. The number of time-dependent permanents $|\mathbf{n};t\rangle$ is $\binom{N+M-1}{N}$. $M = 1$ in the set of permanents, $|\mathbf{n};t\rangle$, of Eq. 2.2 represents the Gross-Pitaevskii ansatz and solves the time-dependent Gross-Pitaevskii equation [69]. The accuracy of the wavefunction increases with M and achieves the convergence of different physical quantities of interest discussed in this work, such as the survival probability, depletion and fragmentation, and the many-particle position, momentum, and angular-momentum variances. The numerical implementation of the real-time dynamics employed in this work can be found in [70, 71].

Here, we investigate the dynamics of a few bosonic clouds prepared as either the ground, transversely-excited or longitudinally-excited state for longitudinal and transversal resonant tunneling phenomena in two different double-well potentials. In case of longitudinal resonant tunneling, we consider that the bosons are initially prepared in the left well,

$$V_L(x,y) = \frac{1}{2}(x+2)^2 + \frac{1}{2}y^2 - cx, \tag{2.3}$$

of a double-well potential, where c is the asymmetry parameter. The bosons are taken in the state of either as the non-interacting ground, $\Psi_G = \frac{1}{\sqrt{\pi}}F(x,y)$, or as the transversely-excited, $\Psi_Y = \sqrt{\frac{2}{\pi}}yF(x,y)$, states, where $F(x,y) = exp[-\{(x+2)^2 + y^2\}/2]$. Fig. 1 shows the initial density distributions of Ψ_G and Ψ_Y. To explore the dynamics of the bosonic clouds, we suddenly quench the inter-particle interaction at $t = 0$ from $\Lambda = 0$ to $\Lambda = 0.01\pi$ and simultaneously change the trapping potential from $V_L(x,y)$ to the longitudinally-asymmetric 2D double-well potential, $V_T(x,y)$. Here the asymmetry implies the right well is lower than the left well. This is achieved by adding a linear term in the longitudinal direction. The mathematical form of $V_T(x,y)$ is (see Fig. 1(a)):

$$V_T(x,y) = \begin{cases} \frac{1}{2}(x+2)^2 + \frac{1}{2}y^2 - cx, & x < -\frac{1}{2}, -\infty < y < \infty, \\ \frac{3}{2}(1-x^2) + \frac{1}{2}y^2 - cx, & |x| \leq \frac{1}{2}, -\infty < y < \infty, \\ \frac{1}{2}(x-2)^2 + \frac{1}{2}y^2 - cx, & x > +\frac{1}{2} - \infty < y < \infty. \end{cases} \tag{2.4}$$

In order to investigate the transversal resonant tunneling phenomenon, we assume the bosons are prepared either as the non-interacting Ψ_G or longitudinally-excited state, $\Psi_X = \sqrt{\frac{2}{\pi}}(x+2)F(x,y)$, in the left well, $V'_L(x,y)$, of a transversely-asymmetric 2D double-well potential, $V'_T(x,y)$. Here the asymmetry means the right well is wider than the left well. This is generated by making the transverse frequency of the trap spatially-dependent. $V'_L(x,y)$ is functioned as

$$V'_L(x,y) = \begin{cases} \frac{1}{2}(x+2)^2 + \frac{1}{2}y^2, & x < -1, -\infty < y < \infty, \\ \frac{1}{2}(x+2)^2 + \frac{1}{2}[S(x)]^2 y^2, & -1 < x < +1, -\infty < y < \infty, \\ \frac{1}{2}(x+2)^2 + \frac{1}{2}\omega_n^2 y^2, & x > +1, -\infty < y < \infty. \end{cases} \tag{2.5}$$

Here, $S(x) = \left[1 + (\omega_n - 1)sin^2\frac{(x+1)\pi}{4}\right]$ is a switching function for the transversal frequency, where ω_n is the minimal value of the transversal frequency. The initial density distribution of Ψ_X is presented in Fig. 1. For investigating the time evolution, as described in the longitudinal resonant tunneling, we quench the inter-particle interaction at $t = 0$ from $\Lambda = 0$ to $\Lambda = 0.01\pi$. At the same time, we convert $V'_L(x,y)$ to the transversely-asymmetric 2D double-well potential $V'_T(x,y)$ (see Fig. 1(b)), where

$$V'_T(x,y) = \begin{cases} \frac{1}{2}(x+2)^2 + \frac{1}{2}y^2, & x < -1, -\infty < y < \infty, \\ \frac{1}{2}(x+2)^2 + \frac{1}{2}[S(x)]^2 y^2, & -1 < x < -\frac{1}{2}, -\infty < y < \infty, \\ \frac{3}{2}(1-x^2) + \frac{1}{2}[S(x)]^2 y^2, & |x| \leq \frac{1}{2}, -\infty < y < \infty, \\ \frac{1}{2}(x-2)^2 + \frac{1}{2}[S(x)]^2 y^2, & \frac{1}{2} < x < 1, -\infty < y < \infty, \\ \frac{1}{2}(x-2)^2 + \frac{1}{2}\omega_n^2 y^2, & x > +1, -\infty < y < \infty \end{cases} \tag{2.6}$$

To accurately tackle the many-body physics involved in the two-dimensional bosonic Josephson junctions, we have performed the MCTDHB computations with different time-dependent orbitals for different initial bosonic structures. For Ψ_G and Ψ_X, the many-body computations are performed with $M = 6$ time-dependent orbitals, while for Ψ_Y with $M = 10$ time-dependent orbitals. The

convergence with the orbital numbers of the quantities discussed in this work are shown in the supplemental materials. For the numerical solution of the longitudinal resonant tunnelling, the considered box size is $[-10, 10) \times [-10, 10)$ with periodic boundary conditions having a grid of 64×64 points and for the transversal resonant tunneling, we increase the grid density to 128×128. Convergence of the results with respect to the number of grid points has been checked and presented in the supplemental materials. Adequacy of the 2D box size for both longitudinal and transversal scenarios have been checked. For the many-body dynamics of both the resonant tunnelings, the number of bosons and interaction parameter are chosen as $N = 10$ and $\Lambda = 0.01\pi$. The mean-field dynamics are also computed with same interaction parameter Λ to relate the results with the respective many-body ones. It is noted that as the considered interparticle interaction in the dynamics is weak, the preparation of the initial state in the relaxation process either with noninteracting bosons or or with $\Lambda = 0.01\pi$ does not affect the dynamical behavior of the properties discussed in this work. The consistency of preparation of the initial state is documented in the supplemental materials of [25]. The natural units $\hbar = m = 1$ are employed throughout this work.

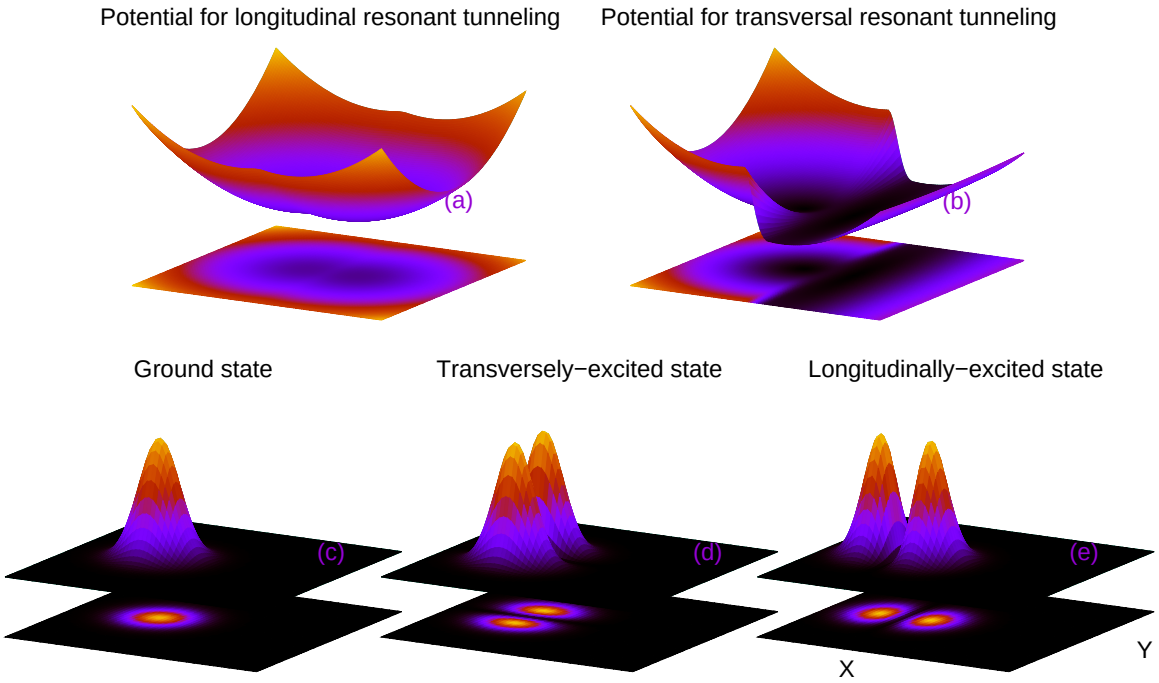

FIG. 1. Schematic diagrams for the asymmetric 2D double-well potential for (a) longitudinal resonant tunneling, described in Eq. 2.4 and (b) transversal resonant tunneling, described in Eq. 2.6. Panels (c), (d), and (e) show the initial density distributions for the ground, transversely-excited, and longitudinally-excited states, respectively. Panel (e) shows the x- and y-axes.

III. RESULTS AND DISCUSSIONS

Here, we divide the section into two parts, namely, longitudinal and transversal resonant tunneling. In each part, we investigate the time evolution of various physical quantities, such as the survival probability, loss of coherence, and the variances of the position, momentum, and angular-momentum many-particle operators when the symmetry of the double-well potential is broken and it reaches to the resonant tunneling condition. The quantities discussed here incorporate a detailed information of the time-dependent many-boson wave function, explicitly, the density, reduced one-particle density matrix, and reduced two-particle density matrix.

A. Longitudinal resonant tunneling

At first we investigate how the longitudinal resonant tunneling phenomena of Ψ_G and Ψ_Y are achieved by gradually increasing the asymmetry parameter, c, in the longitudinally-asymmetric 2D double-well potential described in Eq. 2.4. Further, we discuss the time-evolution of the different physical quantities, mentioned above, for Ψ_G and Ψ_Y at the resonant tunneling condition and compare them with the corresponding results of symmetric 2D double-well potential, which can be obtained at $c = 0$ from Eq. 2.4. The investigation is performed and compared at the mean-field and many-body levels of theory.

In this work, Ψ_G and Ψ_Y are prepared in the left well of a 2D double-well potential. When we gradually increase the value of c starting from zero, the symmetry of the double-well potential breaks and the left well becomes the upper well and, consequently, the right well becomes the lower well. For some special values of c, the one-body energy of the left well coincides with one of the higher one-body energy levels of the right well, resulting in an enhanced tunneling of bosons from the left well to the right well. This enhancement of tunneling is usually referred to as the resonant tunneling in a double-well potential, see in this context [31, 32]. From Eq. 2.4, we can find out that at any asymmetry parameter c, the energy difference of one-body spectrum between the two wells becomes $4c$. Analytically, for harmonic left and right wells, one can realize that the resonant tunneling occurs when $4c$ will be equal to an integer.

Now, we show how the gradual increase of asymmetry between the two wells of a double-well potential influences the tunneling of particles. In Fig. 2, we present, at the mean-field level, the variation of the maximal number of particles tunneling from the left to the right well for the states Ψ_G and Ψ_Y with the asymmetry parameter c. This maximal number of particles in the right well is

determined from $\int_{x=0}^{+\infty}\int_{y=-\infty}^{+\infty} dxdy\frac{\rho(x,y;t)}{N}$, where $\rho(x,y;t)$ is the density of the bosonic cloud. Here, we start from the symmetric double-well potential. At $c=0$, when the bosons are allowed to evolve in time, we observe that 100% of the bosons can tunnel from the left to right well, signifying the delocalization of the one-particle eigen-functions in a symmetric double-well. Now, a small increase of asymmetry between the wells makes the one-particle state to be only partially delocalized over both wells, leading to a suppression of tunneling of particles. Further increase of the asymmetry, beyond $c = 0.1$, the one-particle state slowly begins to be delocalized in one of the wells, and the tunneling of particles increases. At $c = 0.25$, we find well-delocalization of the one-particle state in one of the well which leads to a complete tunneling of particles or specifically, refer to as resonant tunneling condition, when one-body energy of the left well matches with the energy of one of the one-body excited states of the right well. Similarly, the second resonant tunneling appears at $c = 0.5$. As the system is weakly interacting, we find that the maximum tunneling of particles is 100% both for Ψ_G and Ψ_Y at $c = 0$, $c = 0.25$, and $c = 0.5$. Also, we observe a small difference of maximum tunneling of particles between the results of Ψ_G and Ψ_Y at off-resonant tunneling. Here, it is noted that if the bosons are prepared in the right well (lower well), the gradual increase of asymmetry between the wells reduces the maximal number of bosons tunneling to the left well. Further increase of asymmetry between the wells, at $c \gtrsim 0.1$, the bosons become trapped in the right well, and produces only a mild breathing motion, mainly due to the quenching the interaction.

Next, we focus on both the resonant tunneling values of c and study how the many-body correlations affects the dynamical behaviors of the survival probability, loss of coherence, and the many-particle position, momentum, and angular-momentum variances. Moreover, we will display the corresponding analysis of the results obtained for the symmetric double-well potential to serve as a reference. In addition, we will present a comparison study of the mean-field and many-body results both for Ψ_G and Ψ_Y.

In order to adequately capture the time evolutions of Ψ_G and Ψ_Y between the two wells of a double-well potential, we examine the survival probability in the left well, $P_L(t) = \int_{x=-\infty}^{0}\int_{y=-\infty}^{+\infty} dxdy\frac{\rho(x,y;t)}{N}$, where $\rho(x,y;t)$ is the density of the bosonic cloud. We compare between the results of the mean-field and many-body dynamics of $P_L(t)$ in Fig. 3 for the asymmetry parameters, $c = 0$, 0.25, and 0.5. Here, we want to mention that, to have a proper comparison among all the results presented in this paper, the time-scale for the dynamics is set to be equal to the Rabi oscillations (t_{Rabi}) of the symmetric double-well trap (when $c = 0$). We find

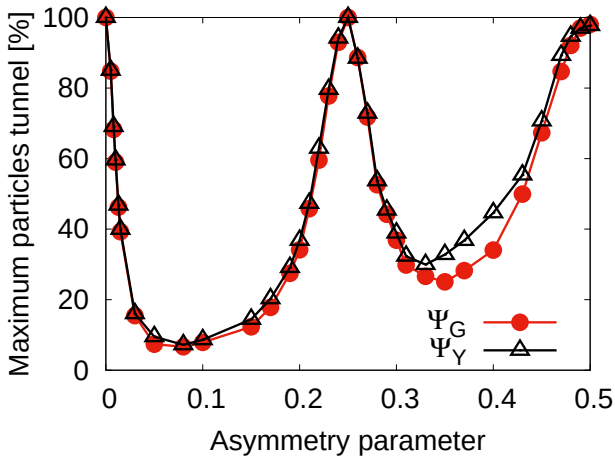

FIG. 2. Variation of the maximal number of particles tunneling [in %] from the left to the right well with the asymmetry parameter c for the states Ψ_G and Ψ_Y at the mean-field level. The data is generated from the time-dependent solution of the Gross-Pitaeveskii equation. We show here dimensionless quantities.

that $t_{Rabi} = 132.498$ for the symmetric 2D double-well potential [25].

In Fig. 3, we observe, for both Ψ_G and Ψ_Y, back and forth of the density between the left and right wells with the essentially same frequency of oscillations at a particular value of c. In the non-interacting system, at $t = 0$, Ψ_G and Ψ_Y lie approximately on the lowest band along the direction of the barrier and when there is an interaction quench, more bands are coupled. Both the frequency and amplitude of the tunneling oscillations of Ψ_G are essentially similar to those of Ψ_Y at the mean-field level. But, at the many-body level, only the frequency of the tunneling oscillations remains very similar for Ψ_G and Ψ_Y at a particular value of c, while the amplitudes show a substantial difference as time progresses. The difference in the many-body tunneling amplitude between Ψ_G and Ψ_Y occurs as more states start to couple with time to Ψ_Y in comparison to Ψ_G. At $c = 0.25$ and 0.5, the ground state energy of the left well matches with energies of the second (which is two-fold degenerate, $x\Psi_G$ and $y\Psi_G$) and third (which is three-fold degenerate, $xy\Psi_G$, $(x^2-1)\Psi_G$, and $(y^2-1)\Psi_G$) excited states of the right well, respectively. But, in the process of tunneling, Ψ_G couples to $x\Psi_G$ and $(x^2-1)\Psi_G$ of the right well at $c = 0.25$ and 0.5, respectively. Similarly, Ψ_Y couples respectively to $x\Psi_Y$ and $(x^2-1)\Psi_Y$ of the right well. As Ψ_G and Ψ_Y mainly couple to those excited states which have excitations only along the x-direction, we call this tunneling the longitudinal resonant tunneling.

For both Ψ_G and Ψ_Y, the short-time mean-field and many-body dynamics of $P_L(t)$ overlap for the interaction strength taken here. This condition imitates the so-called infinite-particle limit of the time-dependent many-boson Schrödinger equation [72, 73]. Contrary to the mean-field

dynamics, one can find a signature of the quantum correlations in the many-body dynamics of $P_L(t)$ in terms of incomplete tunneling of the densities and, consequently, the amplitude of the oscillations of $P_L(t)$ gradually decays. The decay in the amplitude of the many-body $P_L(t)$ signifies a collapse in the density oscillations, which is more pronounced for Ψ_G than for Ψ_Y. However, as c increases, the decay rates of Ψ_G and Ψ_Y become smaller. For a certain value of c, the decay rate of Ψ_G is larger compared to the corresponding rate of Ψ_Y, suggesting that in the tunneling process, the many-body effects develops in a different rate for different initial structures of the bosonic clouds. Explicitly, we observe that having transverse excitation delays the many-body process of the density oscillations collapse. Moreover, at $c = 0.5$, the time evolution of $P_L(t)$ exhibits a partial revival for both the states.

Signature of a growing degree of quantum correlations is already found in terms of decay in the amplitude of the time evolution of many-body $P_L(t)$. Now, we will discuss how this gradual increase of the many-body correlations can affect the coherence of the condensates, i.e., bosonic clouds of Ψ_G and Ψ_Y, when the resonant tunneling occurs. To compare the results, we also show the loss of coherence for the tunneling of the above considered bosonic clouds in the symmetric double-well potential as a reference. In Fig. 4, we present the time evolution of the condensate fraction, $\frac{n_1(t)}{N}$, obtained by diagonalizing the reduced one-particle density matrix of the time-dependent many-boson wave-function (Eq. 2.2) [74, 75]. The general feature of the occupation of the first natural orbital is found to be decreasing with time having a weak oscillatory background for all values of asymmetry parameters. It is observed that Ψ_Y loses coherence faster than Ψ_G for a particular value of c, suggesting that inclusion of the transverse excitation enhances fragmentation in Ψ_Y [25]. We find that the rate of loss of coherence becomes slower when one move from $c = 0$ to the first resonant tunneling value at $c = 0.25$ and further slower at the second resonant tunneling.

In the context of occupations of the first natural orbital, it is worthwhile to mention the occupancy of higher natural orbitals. We find that, as the time passes by and fragmentation of the condensate grows, the occupancy of all higher natural orbitals gradually increases. The occupancy of higher natural orbitals have direct impact on the different many-body quantities discussed later, i.e, on the mechanism of many-body resonant tunneling in 2D double-wells. The detailed process of fragmentation with their convergences are discussed in the supplemental materials.

Having explicated the development of many-body correlations and their effects on the time evolution of the survival probability and coherence of the bosonic clouds, we find further information of the time-dependent many-particle wavefunction and especially, the signature of the depletion and fragmentation on the condensate. As the variance is a sensitive probe of correlation [48], we

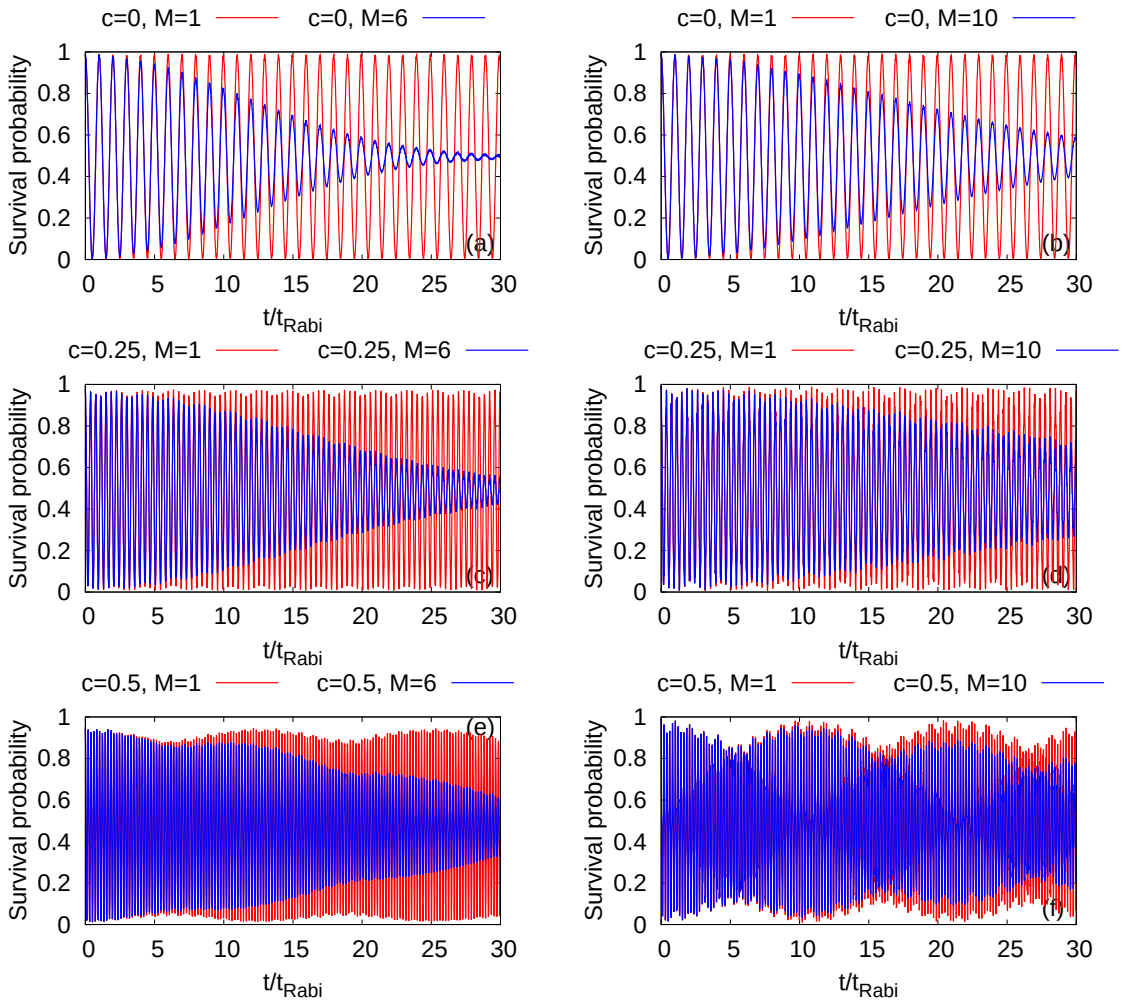

FIG. 3. Dynamics of the survival probability of Ψ_G (left column) and Ψ_Y (right column) in the left well of longitudinally-asymmetric 2D double-well potential of $N = 10$ bosons with the interaction parameter $\Lambda = 0.01\pi$. The first row presents the results for the symmetric double-well potential. Second and third rows show the survival probabilities at the resonant tunneling with asymmetry parameter, $c = 0.25$ and 0.5, respectively. $M = 1$ signifies the mean-field results. The many-body dynamics are computed with $M = 6$ time-dependent orbitals for Ψ_G and $M = 10$ time-dependent orbitals for Ψ_Y. We show here dimensionless quantities. Color codes are explained in each panel.

graphically analyze the dynamical behavior of the variances of a few fundamental quantum mechanical observables which are mostly influenced by the longitudinal resonant tunneling. These are the position and momentum operators along the x-direction, and the angular-momentum operator.

Fig. 5 displays the time evolution of the many-particle position variance per particle along the x-direction, $\frac{1}{N}\Delta^2_{\hat{X}}(t)$, in the longitudinally-asymmetric 2D double-well potential with asymmetry parameters, $c = 0$, 0.25, and 0.5 for the bosonic clouds of Ψ_G and Ψ_Y (see Appendix A for the

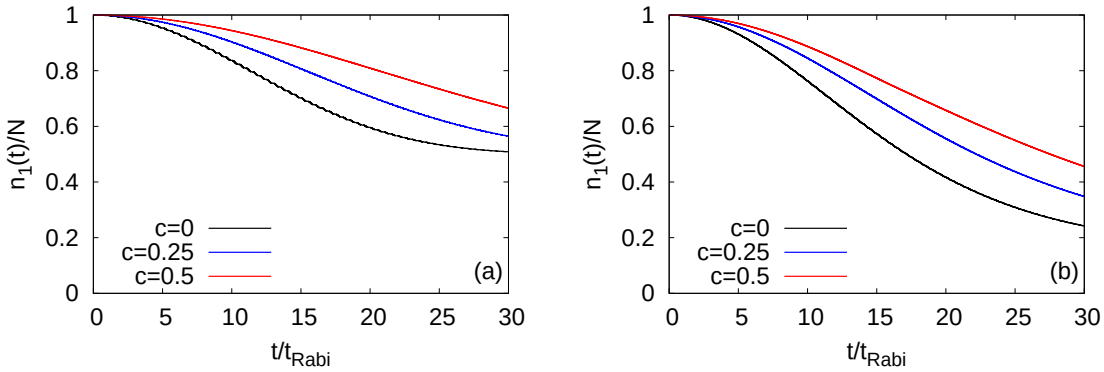

FIG. 4. Time-dependent occupation per particle of the first natural orbital, $\frac{n_1(t)}{N}$, in a longitudinally-asymmetric 2D double-well potential for $N = 10$ bosons and interaction parameter $\Lambda = 0.01\pi$. Panels (a) and (b) are for Ψ_G and Ψ_Y, respectively. The asymmetry parameters are $c = 0$, 0.25, and 0.5. The data have been obtained with $M = 6$ time-dependent orbitals for Ψ_G and $M = 10$ time-dependent orbitals for Ψ_Y. We show here dimensionless quantities. Color codes are explained in each panel.

mathematical form of the many-particle variance and its basic properties). As a general feature, we find that the many-body and mean-field values of $\frac{1}{N}\Delta^2_{\hat{X}}(t)$ are oscillatory in nature. Due to the correlations, the average value of the many-body $\frac{1}{N}\Delta^2_{\hat{X}}(t)$ deviates – it rather significantly increases – from the corresponding mean-field results for all asymmetry parameters and bosonic clouds. Although, we found in Fig. 4 that Ψ_Y is always more fragmented than Ψ_G, the deviations in the values of $\frac{1}{N}\Delta^2_{\hat{X}}(t)$ are always smaller for Ψ_Y compared to Ψ_G at a particular value of c, apart for short-times at $c = 0.5$. Therefore, one can say that the many-body dynamics is complicated and there is no one-to-one correlation between the different many-body properties in the junction, such as fragmentation and $\frac{1}{N}\Delta^2_{\hat{X}}(t)$, but it suggests how the transverse excitations participating in the dynamics can impact the fluctuations in measuring an observable. From the insets of Fig. 5(a) and (b), we find that the peaks of the oscillations of $\frac{1}{N}\Delta^2_{\hat{X}}(t)$ breaks into two sub-peaks which practically turn into two broad peaks at the resonant values of c. Unlike the mean-field dynamics, the many-body $\frac{1}{N}\Delta^2_{\hat{X}}(t)$ oscillates with a growing amplitude until it reaches an equilibrium value which is more evident at $c = 0$ for both the states and at $c = 0.25$ for Ψ_G. This equilibrium value of $\frac{1}{N}\Delta^2_{\hat{X}}(t)$ is reached when the density oscillations collapse as observed in the time evolutions of $P_L(t)$ in Fig. 3. At $c = 0.5$, we notice that the amplitude of the oscillations of $\frac{1}{N}\Delta^2_{\hat{X}}(t)$ are also oscillatory, more pronouncedly for Ψ_Y, which is consistent with the density oscillations. In the dynamics of $\frac{1}{N}\Delta^2_{\hat{X}}(t)$, we observe two kinds of oscillations, i.e., small frequency with large amplitude and high frequency with small amplitude oscillations. The former one comes from the

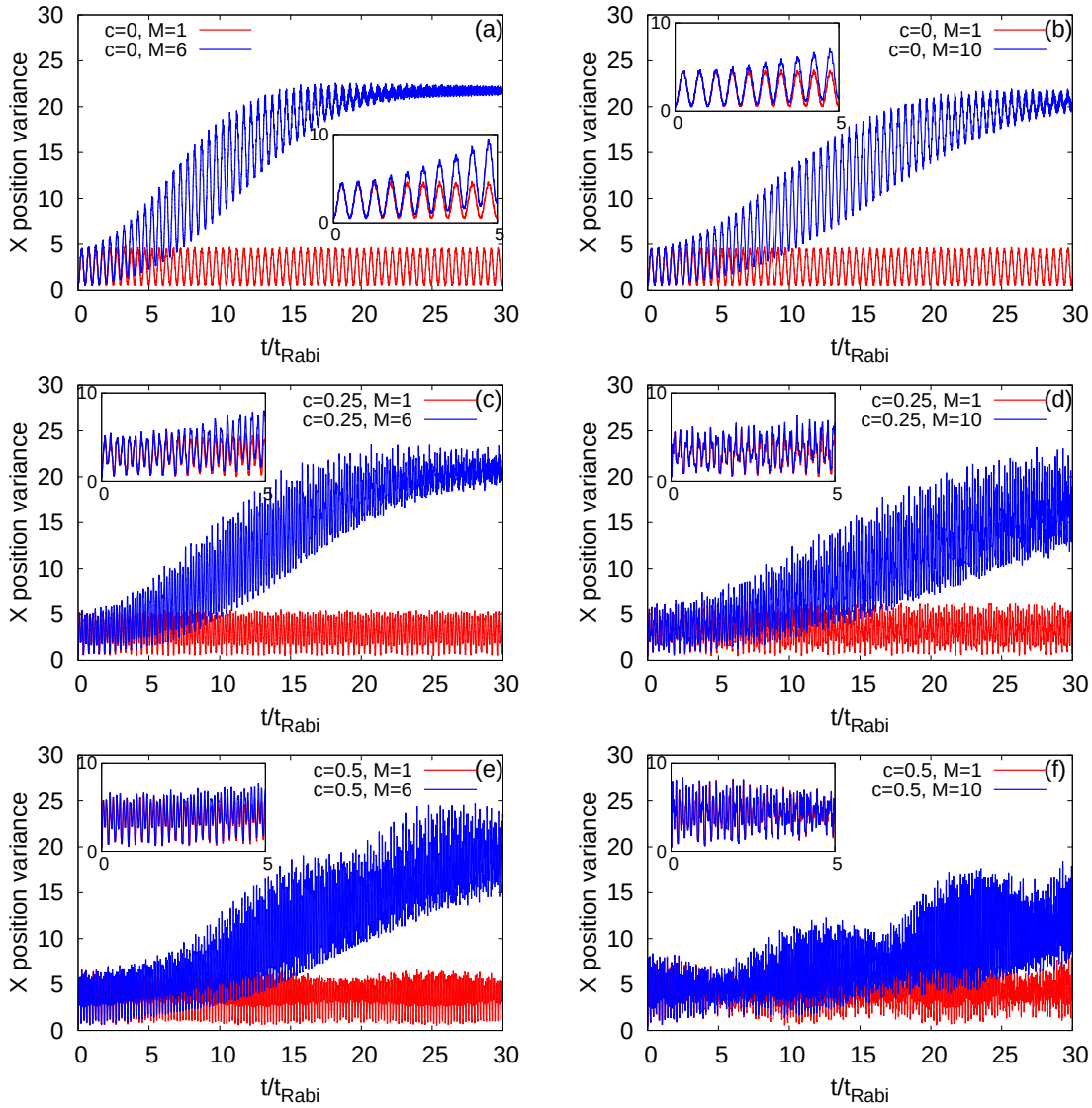

FIG. 5. Time-dependent position variance per particle along the x-direction, $\frac{1}{N}\Delta^2_{\hat{X}}(t)$, in a longitudinally-asymmetric 2D double-well potential for Ψ_G (left column) and Ψ_Y (right column) of $N = 10$ bosons with the interaction parameter $\Lambda = 0.01\pi$. The first row presents the results for the symmetric double-well potential. The second and third rows show $\frac{1}{N}\Delta^2_{\hat{X}}(t)$ at the resonant tunneling with asymmetry parameter, $c = 0.25$ and 0.5, respectively. $M = 1$ signifies the mean-field results. The many-body dynamics are computed with $M = 6$ time-dependent orbitals for Ψ_G and $M = 10$ time-dependent orbitals for Ψ_Y. From $t = 0$ to $5t_{Rabi}$ timescale of $\frac{1}{N}\Delta^2_{\hat{X}}(t)$ is highlighted in the inset of each panel. We show here dimensionless quantities. Color codes are explained in each panel.

density oscillations and the latter one occurs due to the breathing-mode oscillations of the system. At the resonant values of c, the high frequency with small amplitude oscillations are more clearly visible.

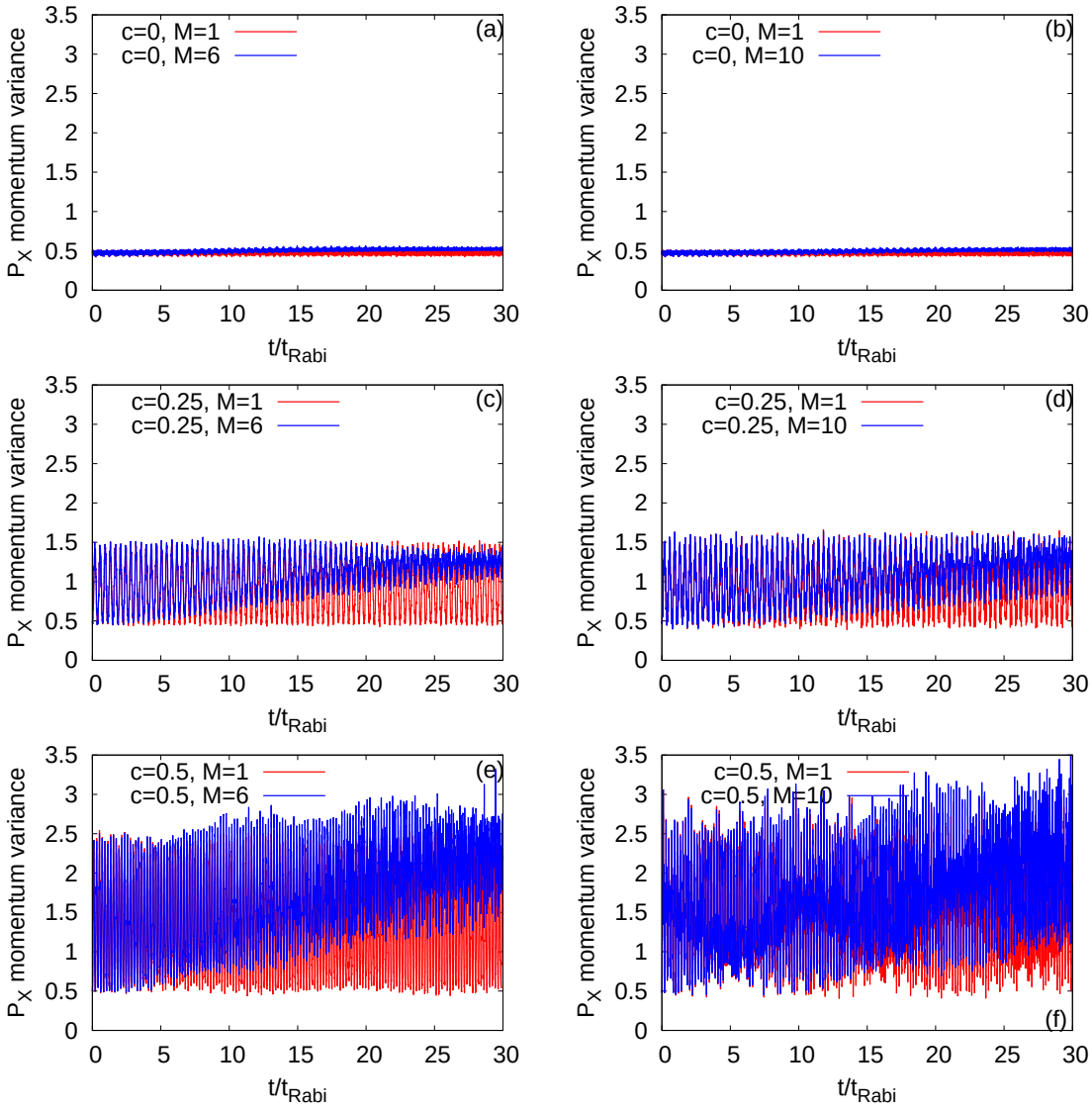

FIG. 6. Time-dependent momentum variance per particle along the x-direction, $\frac{1}{N}\Delta^2_{\hat{P}_X}(t)$, in a longitudinally-asymmetric 2D double-well potential for Ψ_G (left column) and Ψ_Y (right column) of $N = 10$ bosons with the interaction parameter $\Lambda = 0.01\pi$. The first row presents the results for the symmetric double-well potential. The second and third rows show $\frac{1}{N}\Delta^2_{\hat{P}_X}(t)$ at the resonant tunneling with asymmetry parameter, $c = 0.25$, and 0.5, respectively. $M = 1$ signifies the mean-field results. The many-body dynamics are computed with $M = 6$ time-dependent orbitals for Ψ_G and $M = 10$ time-dependent orbitals for Ψ_Y. We show here dimensionless quantities. Color codes are explained in each panel.

Next, we consider the momentum variance per particle along the x-direction, $\frac{1}{N}\Delta^2_{\hat{P}_X}(t)$, and present its time evolution at the mean-field and many-body levels for Ψ_G and Ψ_Y in Fig. 6. We explicitly show the possible quantum correlations effects on the many-body dynamics of $\frac{1}{N}\Delta^2_{\hat{P}_X}(t)$ at the resonant tunneling condition and compare with the corresponding results obtained for the

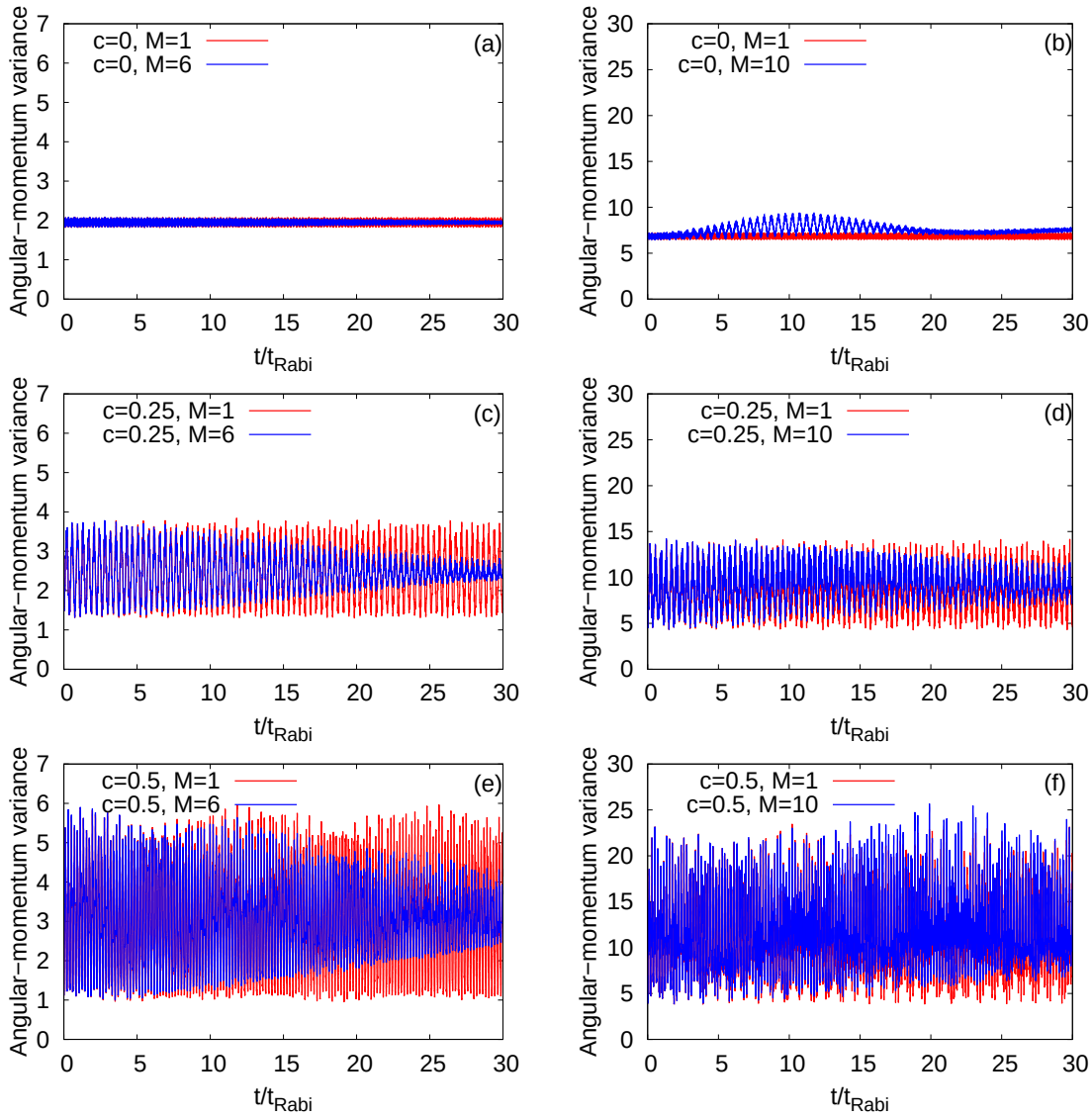

FIG. 7. Time-dependent variance per particle of the z- component of the angular-momentum operator, $\frac{1}{N}\Delta^2_{\hat{L}_Z}(t)$, in a longitudinally-asymmetric 2D double-well potential for Ψ_G (left column) and Ψ_Y (right column) of $N = 10$ bosons with the interaction parameter $\Lambda = 0.01\pi$. The first row presents the results for the symmetric double-well potential. The second and third rows show $\frac{1}{N}\Delta^2_{\hat{L}_Z}(t)$ at the resonant tunneling with asymmetry parameter, $c = 0.25$ and 0.5, respectively. $M = 1$ signifies the mean-field results. The many-body dynamics are computed with $M = 6$ time-dependent orbitals for Ψ_G and $M = 10$ time-dependent orbitals for Ψ_Y. We show here dimensionless quantities. Color codes are explained in each panel.

symmetric double-well potential. Recall that $\frac{1}{N}\Delta^2_{\hat{P}_X}(t)$ is relatively a more complex quantity than $\frac{1}{N}\Delta^2_{\hat{X}}(t)$ in the junction as the former one is controlled by and more sensitive to the shape of the orbitals. In Fig. 6, we observe, also for $\frac{1}{N}\Delta^2_{\hat{P}_X}(t)$, two types of oscillations, smaller amplitude with higher frequency and larger amplitude with lower frequency. But there is a difference with respect

to $\frac{1}{N}\Delta^2_{\hat{X}}(t)$. For the symmetric double-well potential, $\frac{1}{N}\Delta^2_{\hat{P}_X}(t)$ is dominated by the breathing mode oscillations which produce small amplitude with high frequency oscillations. While at the first resonant tunneling, $c = 0.25$, the density oscillations are more prominent producing the larger amplitude but lower frequency oscillations. But, at the second resonant tunneling, $c = 0.5$, $\frac{1}{N}\Delta^2_{\hat{P}_X}(t)$ shows a mixture of the density and breathing mode oscillations. At $c = 0.25$, the mean-field $\frac{1}{N}\Delta^2_{\hat{P}_X}(t)$ oscillates between 0.5 and 1.5, while at $c = 0.5$, between 0.5 and 2.5. This reflects the ground (left well) and excited (right well) orbitals participating in the dynamics. One of the interesting features at the resonant tunneling condition is that the minima values of the many-body $\frac{1}{N}\Delta^2_{\hat{P}_X}(t)$ increases with the growing degree of fragmentation. Also, the amplitude of the many-body oscillations of $\frac{1}{N}\Delta^2_{\hat{P}_X}(t)$ eventually decays, which is clearly visible at $c = 0.25$, when the density collapses. It suggests that in the long-time dynamics of $\frac{1}{N}\Delta^2_{\hat{P}_X}(t)$, the excited state in the right well slowly wins over the initial state prepared in the left well.

In this context, it is worthwhile to briefly discuss the position and momentum variances along the y-direction, $\frac{1}{N}\Delta^2_{\hat{Y}}(t)$ and $\frac{1}{N}\Delta^2_{\hat{P}_Y}(t)$, respectively. We found in our work that the mean-field and many-body values of $\frac{1}{N}\Delta^2_{\hat{Y}}(t)$ and $\frac{1}{N}\Delta^2_{\hat{P}_Y}(t)$ have very small fluctuations, of the order of 10^{-3}, atop the value of the non-interacting bosons, i.e., 0.5 and 1.5 for both variances, for Ψ_G and Ψ_Y, respectively (see supplemental materials). Also, with the change in asymmetry parameter, we do not observe any substantial changes in the values of position and momentum variances along the transverse direction. However, in addition to the motion along the x-direction, the effect of the seemingly constant transverse degrees-of-freedom lead to the existence of a purely two-dimensional quantity, such as the angular-momentum.

Now, we examine the angular-momentum variance per particle, $\frac{1}{N}\Delta^2_{\hat{L}_Z}(t)$, and demonstrate the implications of the resonant tunneling on its dynamical behavior in Fig. 7, see Appendix A for the mathematical form of $\frac{1}{N}\Delta^2_{\hat{L}_Z}(t)$. The results are compared at the mean-field and many-body levels for Ψ_G and Ψ_Y. At $t = 0$, in case of the symmetric double-well trap, $\frac{1}{N}\Delta^2_{\hat{L}_Z}(t)$ can be calculated analytically and is found to be 2 and 7 for Ψ_G and Ψ_Y, respectively. At the first and second resonant tunneling, the initial values of $\frac{1}{N}\Delta^2_{\hat{L}_Z}(t)$ for Ψ_G are reduced to 1.5 and and 1, respectively. But for Ψ_Y, $\frac{1}{N}\Delta^2_{\hat{L}_Z}(t)$ remains 7 at $t = 0$ for the resonant values of c. For the symmetric double-well potential, we find that $\frac{1}{N}\Delta^2_{\hat{L}_Z}(t)$ of Ψ_G oscillates with amplitude of fluctuations in the order of 10^{-1} at the mean-field level. A rather small difference, marking the collapse of the density oscillations, is present between the time evolutions of $\frac{1}{N}\Delta^2_{\hat{L}_Z}(t)$ at the mean-field and many-body levels. Unlike for Ψ_G, interesting many-body features are found

for Ψ_Y at $c = 0$. It is noticed that the amplitude of the many-body $\frac{1}{N}\Delta^2_{\hat{L}_Z}(t)$ of Ψ_Y initially grows and, as time passes by, it decays (at around $t = 12t_{Rabi}$) for the symmetric double-well potential. The maximal fluctuations on top of the baseline of $\frac{1}{N}\Delta^2_{\hat{L}_Z}(t)$ at the many-body level is 34% where as at the mean-field level it is 7%. Contrary to the symmetric double-well potential, at resonant tunneling, the angular-momentum variance shows a sudden increase in the amplitude both for Ψ_G and Ψ_Y. The mean-field and many-body dynamics of $\frac{1}{N}\Delta^2_{\hat{L}_Z}(t)$ are oscillatory in nature at the resonant tunneling values of c. At $c = 0.25$, the mean-field $\frac{1}{N}\Delta^2_{\hat{L}_Z}(t)$ oscillates between 1.5 and about 3.5 for Ψ_G and, between 5 and about 13 for Ψ_Y. At the second resonant tunneling, the amplitude of the mean-field of $\frac{1}{N}\Delta^2_{\hat{L}_Z}(t)$ further increases and oscillates between 1 and approximately 6 for Ψ_G, and between 5 and approximately 22 for Ψ_Y. We notice that Ψ_Y has always larger fluctuations of amplitude of $\frac{1}{N}\Delta^2_{\hat{L}_Z}(t)$ compared to Ψ_G at a fixed value of c. The many-body $\frac{1}{N}\Delta^2_{\hat{L}_Z}(t)$ overlaps with the corresponding mean-field results at short time scales and shows a decay in amplitude as fragmentation grows, which is more evident at $c = 0.25$. The rate of decay of $\frac{1}{N}\Delta^2_{\hat{L}_Z}(t)$ values is slower for Ψ_Y, which is consistent with the survival probability and $\frac{1}{N}\Delta^2_{\hat{P}_X}(t)$.

Until now, we determined the effect of the transverse excitations on the dynamics of Ψ_G and Ψ_Y at the resonant tunneling condition within the mean-field and many-body levels of theory. The effects of the transverse degrees-of-freedom are analyzed in terms of various physical quantities. The results prove that the transverse direction have substantial influences on the dynamics of the ground as well as excited states at the longitudinal resonant tunneling scenario in two spatial dimensions.

B. Transversal resonant tunneling

Proceeding to the transversal resonant tunneling, we want to emphasize that this scenario does only exist in 2D, thereby bringing to the front new degrees-of-freedom with the transverse direction, which we would like to explore. We have found that transverse excitations play a substantial role in longitudinal resonant tunneling. Here, we ask how and in what capacity longitudinal excitations play a role in transversal resonant tunneling.

At first, we examine how the transversal resonant tunneling can be achieved for two initial bosonic structures, Ψ_G and Ψ_X, in a transversely-asymmetric 2D double-well potential presented in Eq. 2.6. Here, we gradually decrease the transverse frequency in the right well, ω_n, from an initial

value ($\omega_n = 1$) which represents a symmetric double-well potential. Similarly to the longitudinal resonant tunneling, here also, the initial states are prepared in the left well of the double-well potential. Fig. 8 presents the maximal number of particles tunneling to the right well for Ψ_G and Ψ_X. The maximal number is extracted from the time-dependent solution of the Gross-Pitaeveskii equation using $\int_{x=0}^{+\infty}\int_{y=-\infty}^{+\infty} dxdy\frac{\rho(x,y;t)}{N}$, where $\rho(x,y;t)$ is the density of the bosonic cloud. One can see from Fig. 8, at $\omega_n = 1$, that the maximal number of particles tunneling to the right well is 100%. Decreasing the value of ω_n reduces the number of maximum particles which can tunnel to the right well for both initial bosonic clouds. The rate of decay of the maximal number of particles tunneling to the right well with ω_n is smaller for Ψ_X as it essentially lies in the first excited band along the direction of the barrier and thus feels a smaller barrier when it tunnels. Further decrease of ω_n, the maximal number of particles tunneling to the right well grows. When the one-body energy of the left well coincides with one of the one-body higher energy levels of the right well, again the maximal number of particles tunneling to the right well reaches to almost 100%. We find only one resonant tunneling for the span of ω_n considered here. For Ψ_G and Ψ_X, the transversal resonant tunneling occurs at $\omega_n = 0.19$ and $\omega_n = 0.18$, respectively. Also, it can be observed from the figure that for slightly off-resonant values of ω_n, the maximal number of particles tunneling to the right well significantly decreases in comparison to the respective value of ω_n at resonant tunneling for Ψ_G, but it varies much weaker with ω_n for ψ_X.

The transversal resonant tunneling for Ψ_G found in Fig. 8 is when Ψ_G of the left well couples to $(y^2-1)\Psi_G$ of the right well. Similarly, Ψ_X of the left well couples to $(y^2-1)\Psi_X$ of the right well to facilitate the transversal resonant tunneling of Ψ_X, see Fig. 9. The resonant tunneling channels $\Psi_G \to y\Psi_G$ and $\Psi_X \to y\Psi_X$ are symmetry forbidden, at least at the mean-field level, as the time-dependent orbital becomes odd with respect to $y \to -y$. Here we select three values of ω_n which are either at the resonant tunneling value or close to it, say, $\omega_n = 0.18$, 0.19, and 0.20, and investigate the overall dynamical response through the surviaval probability, loss of coherence, and the variances of position, momentum, and angular-momentum operators. To show the effects of the many-body correlations on different physical quantities, we compare the results of many-body dynamics with corresponding results at the mean-field level.

Now, we start with the discussion of the density oscillations in terms of the survival probability in the left well for both the states Ψ_G and Ψ_X. Fig. 10(c) and (f) show the dynamical behaviors of the survival probabilities at the resonant tunneling conditions for Ψ_G and Ψ_X, respectively. We notice that the frequencies of tunneling of the density between the left and right wells are different for Ψ_G but are essentially same for Ψ_X for different ω_n considered here. At $\omega_n = 0.18$, 0.19, and

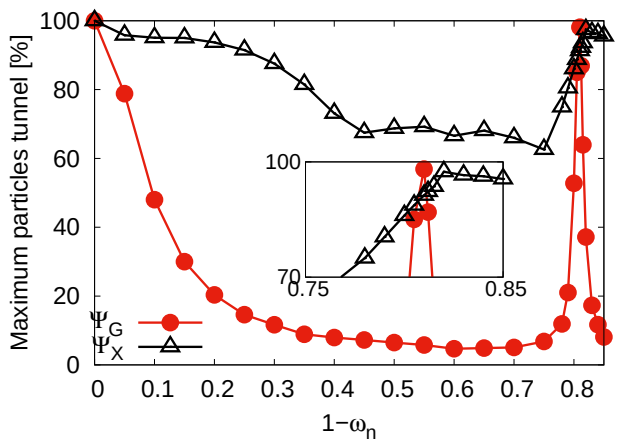

FIG. 8. Variation of the maximal number of particles tunneling [in %] from the left to the right well with the trapping ω_n of the right well for Ψ_G and Ψ_X (see Fig. 1(b)). The interaction parameter is $\Lambda = 0.01\pi$. The same plot is highlighted in the inset by enlarging the resonance region. The data is generated from the time-dependent solution of the Gross-Pitaeveskii equation. We show here dimensionless quantities.

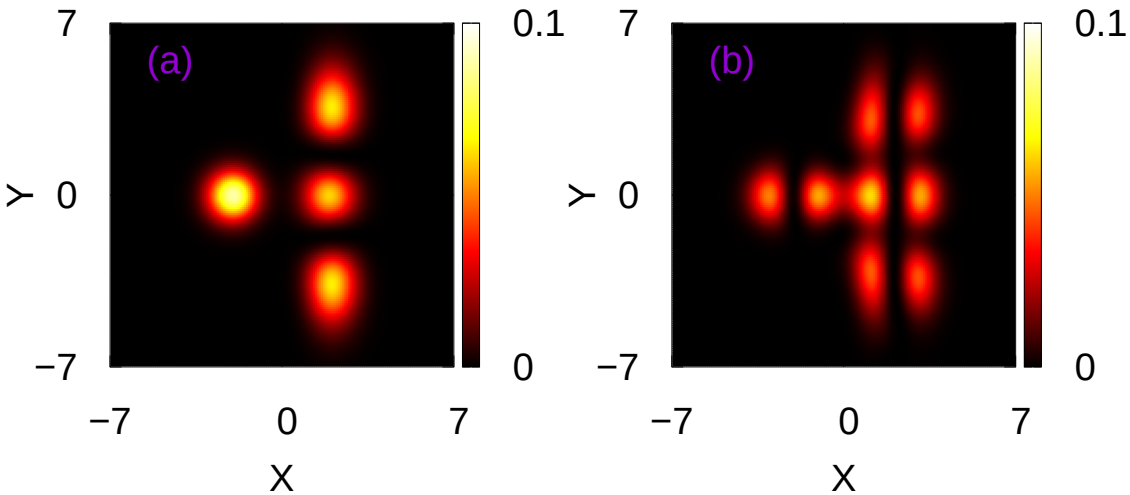

FIG. 9. The densities per particle for the initial states (a) Ψ_G and (b) Ψ_X. The interaction parameter is $\Lambda = 0.01\pi$. The plots are generated at $t \approx t_{Rabi}$ from the time-dependent solution of the Gross-Pitaeveskii equation. We show here dimensionless quantities.

0.20, the tunneling frequencies for Ψ_G are $1.41t_{Rabi}$, $2.30t_{Rabi}$, and $1.55t_{Rabi}$, respectively. While for Ψ_X, the tunneling frequency is around $0.38t_{Rabi}$ for all three ω_n values.

At a fixed value of ω_n, both the frequency and amplitude of the survival probability at the mean-field and many-body levels are practically the same for Ψ_X. Whereas for Ψ_G, although the frequency of the survival probability are very similar at the mean-field and many-body levels, the amplitudes of the survival probability show a significant deviation which is a maximal at

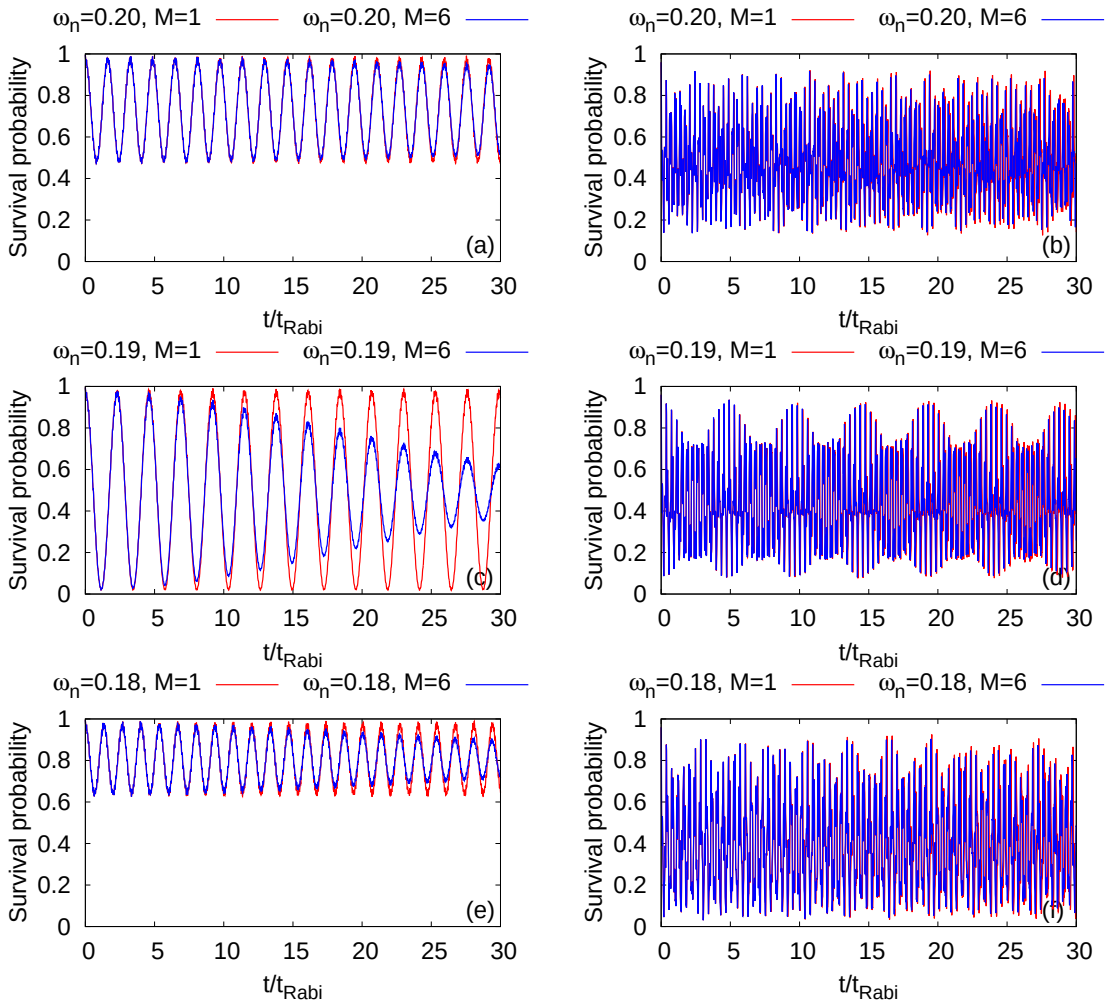

FIG. 10. Dynamics of the survival probability of Ψ_G (left column) and Ψ_X (right column) in the left well of a transversely-asymmetric 2D double-well potential of $N = 10$ bosons with the interaction parameter $\Lambda = 0.01\pi$. First, second, and third rows show the results at frequency, $\omega_n = 0.20$, 0.19, and 0.18, respectively. $M = 1$ signifies the mean-field results. The many-body dynamics are computed with $M = 6$ time-dependent orbitals. We show here dimensionless quantities. Color codes are explained in each panel.

$\omega_n = 0.19$. The gradual decay at the many-body level of dynamics of the survival probability signifies the growing degree of quantum correlations which will be quantitatively discussed later in terms of the loss of coherence in the system. All in all, Fig. 10 reflects that correlations develops faster for Ψ_G compared to Ψ_X.

Now, we demonstrate the effect of growing degree of correlations on the loss of coherence of the bosonic clouds, Ψ_G and Ψ_X, at the transversal resonant tunneling and also at its vicinity. In Fig. 11, we display the time-dependent occupation of the first natural orbital, namely the condensate fraction, $\frac{n_1(t)}{N}$. As observed in the longitudinal resonant tunneling, here also, $\frac{n_1(t)}{N}$

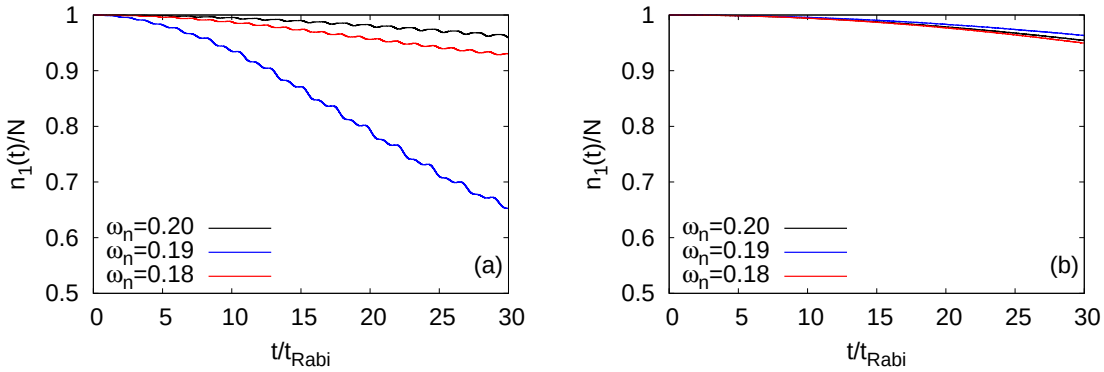

FIG. 11. Time-dependent occupation per particle of the first natural orbital, $\frac{n_1(t)}{N}$, in a transversely-asymmetric 2D double-well potential. The number of bosons is $N = 10$ and the interaction parameter $\Lambda = 0.01\pi$. Panels (a) and (b) are for Ψ_G and Ψ_X, respectively. The data have been obtained with $M = 6$ time-dependent orbitals. We show here dimensionless quantities. Color codes are explained in each panel.

decays with time with a weak oscillatory background. As Ψ_G lies in the lowest band, it feels the barrier more and yields comparatively strong background oscillations than Ψ_X. It is observed that both states lose their coherence faster at the resonant value of ω_n and the loss of coherence becomes gradually slower away from the resonant tunneling. The loss of coherence at the resonant tunneling are seen to be almost 35% and 5% for Ψ_G and Ψ_X, respectively, at the maximum time ($t = 30t_{Rabi}$) considered here. Side by side, the loss of coherence in the system is accompanied by a growing degree of fragmentation, leading to increase of the occupancy of higher natural orbitals. See the supplemental materials for the detailed analysis of the mechanism of fragmentation in transversal resonant tunneling as well as to verification of convergence.

To further characterize the many-body correlations at the transversal resonant tunneling condition for Ψ_G and Ψ_X, we graphically present the dynamical behavior of the variances of the position and momentum operators along the x- and y-directions, and the angular-momentum operator. Also, the many-body results are compared with the corresponding mean-field results. These physical quantities at other values of ω_n, i.e., 0.18 and 0.20 for Ψ_G and 0.19 and 0.20 for Ψ_X, along with their convergences are demonstrated in the supplemental materials.

Fig. 12 displays the dynamics of the many-particle position and momentum variances per particle along the x-direction, $\frac{1}{N}\Delta^2_{\hat{X}}(t)$ and $\frac{1}{N}\Delta^2_{\hat{P}_X}(t)$, respectively, at the transversal resonant tunneling conditions of Ψ_G and Ψ_X. The panels show that the fragmentation developed in the system yields the deviation of the many-body results compared to the corresponding mean-field one. This deviation is larger for Ψ_G in comparison with Ψ_X, which is consistent with the corresponding sur-

vival probability. For Ψ_G, the many-body dynamics of $\frac{1}{N}\Delta^2_{\hat{X}}(t)$ and $\frac{1}{N}\Delta^2_{\hat{P}_X}(t)$ almost reach at its equilibrium when the density oscillations collapse. It is found that the frequency of oscillations is practically the same for the mean-field and many-body dynamics of $\frac{1}{N}\Delta^2_{\hat{X}}(t)$ and $\frac{1}{N}\Delta^2_{\hat{P}_X}(t)$. As we have seen in the dynamics of the survival probability, the oscillation frequency of both quantities is higher for Ψ_X compared to Ψ_G. Moreover, both for Ψ_G and Ψ_X, we find that the frequency of oscillations of the survival probability is twice the frequency of oscillations of $\frac{1}{N}\Delta^2_{\hat{X}}(t)$ while they are practically identical for $\frac{1}{N}\Delta^2_{\hat{P}_X}(t)$. An interesting many-body feature is observed for Ψ_G in the time evolution of $\frac{1}{N}\Delta^2_{\hat{X}}(t)$. Here, we find that there are two types of oscillations taking place, namely, one with high amplitude and the second with a small amplitude. This type of oscillations may arise due to the transition of bosons from the lower to higher band, which requires a detailed analysis, e.g. by a many-body linear-response theory [76], which goes beyond the scope of the present work. The time evolution of $\frac{1}{N}\Delta^2_{\hat{P}_X}(t)$ is accompanied by two types of oscillations, smaller amplitude with higher frequency and larger amplitude with lower frequency, but is mostly dominated by the former one which is coming from the breathing mode oscillations.

Now, let us discuss the role played by the transversal resonant tunneling of Ψ_G and Ψ_X on the time evolution of the position and momentum variances along the y-direction, $\frac{1}{N}\Delta^2_{\hat{Y}}(t)$ and $\frac{1}{N}\Delta^2_{\hat{P}_Y}(t)$, respectively (see Fig. 13). Unlike in the longitudinal resonant tunneling where the position and momentum variances along the y-direction of Ψ_G have very small fluctuations in amplitude (of the order of 10^{-3}, see Fig. S4 in the supplemental materials), here, in the transversal resonant tunneling, we observe comparatively large fluctuations which are clearly more prominent for $\frac{1}{N}\Delta^2_{\hat{Y}}(t)$. For both the states, Ψ_G and Ψ_X, it is found that the frequency of oscillation of $\frac{1}{N}\Delta^2_{\hat{Y}}(t)$ overlaps with the corresponding frequency of the survival probability. The amplitude of the many-body time evolution of $\frac{1}{N}\Delta^2_{\hat{Y}}(t)$ decays with time, originating from the growing degree of fragmentation which is more evident for Ψ_G. It is clear from Fig. 13 that $\frac{1}{N}\Delta^2_{\hat{Y}}(t)$ is dominated by the density oscillations while $\frac{1}{N}\Delta^2_{\hat{P}_Y}(t)$ by the breathing oscillations. We notice that, for Ψ_G, the transversal resonant tunneling gives rise to a beating pattern in the many-body dynamics of $\frac{1}{N}\Delta^2_{\hat{Y}}(t)$ and $\frac{1}{N}\Delta^2_{\hat{P}_Y}(t)$. This beating pattern may be the consequence of the combination of different breathing frequencies. A dedicate study of many-body excitations in the transversely-asymmetric 2D double-well potential could resolve the many-boson states.

Proceeding, we examine the time evolution of the angular-momentum variance per particle, $\frac{1}{N}\Delta^2_{\hat{L}_Z}(t)$, for Ψ_G and Ψ_X at the transversal resonant tunneling scenario (see Fig. 14). The mean-

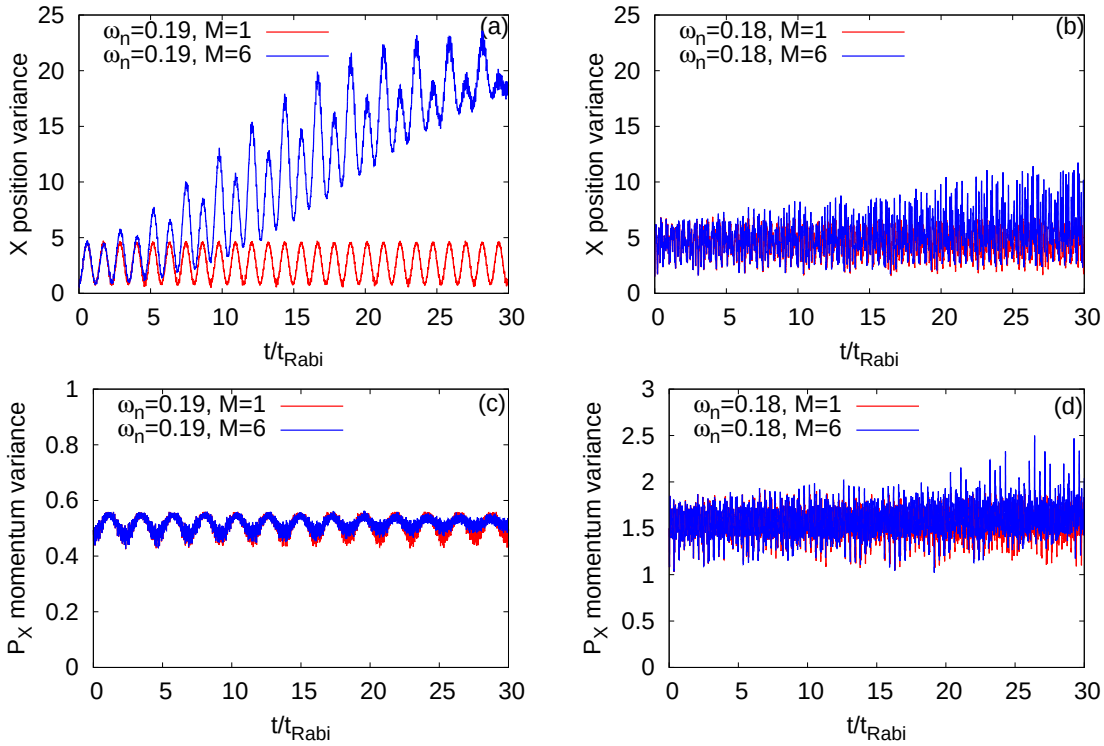

FIG. 12. Time-dependent position and momentum variances per particle along the x-direction in a transversely-asymmetric 2D double-well potential for Ψ_G (left column, $\omega_n = 0.19$) and Ψ_X (right column, $\omega_n = 0.18$) under transversal resonant tunneling conditions. The number of bosons is $N = 10$ and the interaction parameter $\Lambda = 0.01\pi$. $M = 1$ signifies the mean-field results. The many-body dynamics are computed with $M = 6$ time-dependent orbitals. We show here dimensionless quantities. Color codes are explained in each panel.

field dynamics of $\frac{1}{N}\Delta^2_{\hat{L}_Z}(t)$ for Ψ_G showcases smooth undulations and it is uneven for Ψ_X which is consistent with the survival probabilities of the corresponding states. The amplitude of the oscillations of the mean-field $\frac{1}{N}\Delta^2_{\hat{L}_Z}(t)$ of Ψ_X is larger compared to Ψ_G, as one can see in panels (a) and (b) of Fig. 14. For both states, we notice that the frequency of the oscillations of $\frac{1}{N}\Delta^2_{\hat{L}_Z}(t)$ overlaps with the corresponding frequency of $\frac{1}{N}\Delta^2_{\hat{Y}}(t)$. The growing degree of the fragmentation causes a decay in amplitude of the many-body $\frac{1}{N}\Delta^2_{\hat{L}_Z}(t)$ which is significantly more prominent for Ψ_G and hardly visible for Ψ_X.

IV. SUMMARY AND CONCLUSIONS

The paradigm of a bosonic Josephson junction, in which bosons can tunnel back and forth between two potential wells, is shown to be very rich at resonant tunneling condition in two spatial

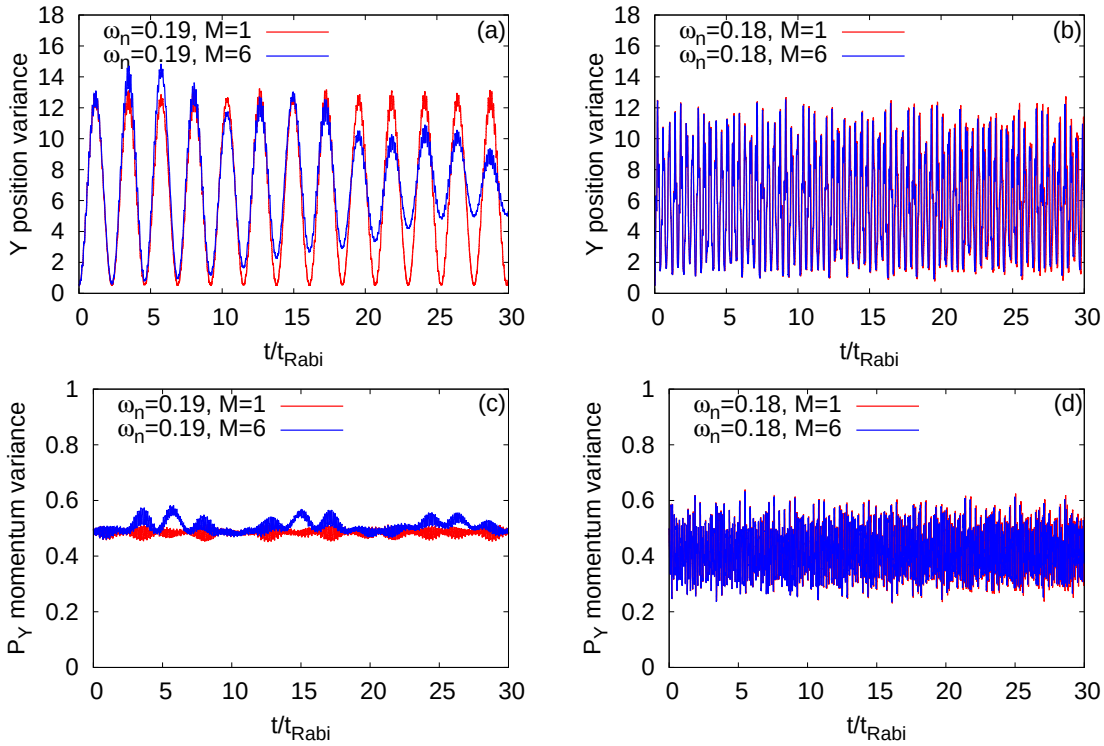

FIG. 13. Time-dependent position and momentum variance per particle along the y-direction in a transversely-asymmetric 2D double-well potential for Ψ_G (left column, $\omega_n = 0.19$) and Ψ_X (right column, $\omega_n = 0.18$) under transversal resonant tunneling conditions. The number of bosons is $N = 10$ and the interaction parameter $\Lambda = 0.01\pi$. $M = 1$ signifies the mean-field results. The many-body dynamics are computed with $M = 6$ time-dependent orbitals. We show here dimensionless quantities. Color codes are explained in each panel.

dimensions. We have investigated the dynamical behavior of a few intricate coherent bosonic clouds at resonant tunneling conditions in a two-dimensional asymmetric Josephson junction. In particular, we examine two types of resonant tunnelings, longitudinal and transversal. For the longitudinal resonant tunneling, the initial bosonic clouds are considered as the ground and transversely-excited states, whereas for transversal resonant tunneling, they are taken as the ground and longitudinally-excited states. The excited states are considered in such a way that we can explore the impact of longitudinal resonant tunneling on the transversely-excited state and analogously, transversal resonant tunneling on the longitudinally-excited state. The dynamical behavior is analyzed by solving the full many-body Schrödinger equation and presenting the time evolution of the survival probability, depletion or fragmentation, and the many-particle position, momentum, and angular momentum variances. To characterize the influence of the many-body correlations on the tunneling dynamics of the different shapes of the bosonic clouds, we compare the mean-field and many-body

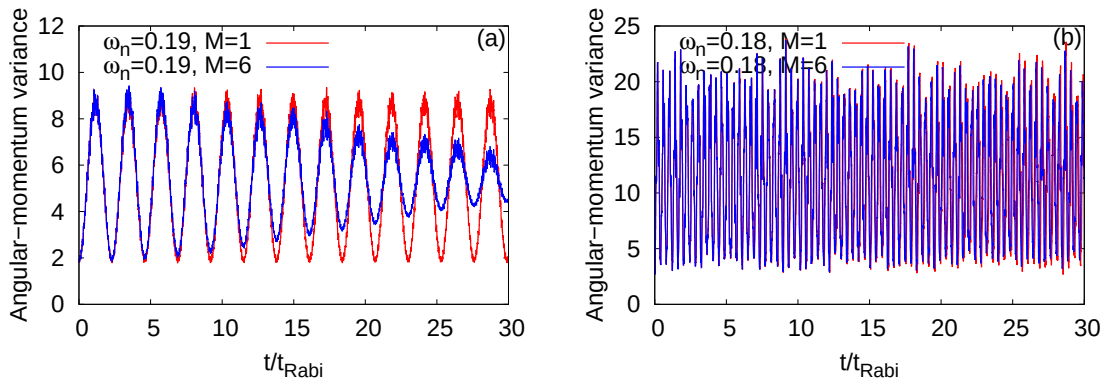

FIG. 14. Time-dependent variance per particle of the z- component of the angular-momentum operator, $\frac{1}{N}\Delta^2_{L_z}(t)$, in a transversely-asymmetric 2D double-well potential for Ψ_G (left column, $\omega_n = 0.19$) and Ψ_X (right column, $\omega_n = 0.18$) under transversal resonant tunneling conditions. The number of bosons is $N = 10$ and the interaction parameter $\Lambda = 0.01\pi$. $M = 1$ signifies the mean-field results. The many-body dynamics are computed with $M = 6$ time-dependent orbitals. We show here dimensionless quantities. Color codes are explained in each panel.

results.

Focusing on the longitudinal resonant tunneling scenario, we verify that a gradual change of asymmetry parameter c either from the values of resonant tunnelings, or the value for which one gets the symmetric double-well potential, decreases the tunneling probability of the bosons. The many-body correlations exhibit the collapse of the density oscillations which is manifested in the dynamics of the survival probability. The collapse rate becomes slower when one moves away from the symmetric double-well potential to the first longitudinal resonant tunneling condition ($c = 0.25$) and further slower toward the second longitudinal resonant tunneling condition ($c = 0.5$). Moreover, at $c = 0.5$ we find a partial revival pattern in the mean-field as well as the many-body survival probabilities. Although the rate of collapse of density oscillation for Ψ_Y is slower compared to Ψ_G at a fixed value of c, the presence of transverse excitation in Ψ_Y makes it more fragmented than Ψ_G at a given time. Compared to the symmetric double-well potential, we observe that both initial states become less fragmented at $c = 0.25$ and further less fragmented at $c = 0.5$.

Referring to the transversal resonant tunneling scenario, we scan the frequency along the transverse direction in the right well, ω_n, starting from the value $\omega_n = 1$ (symmetric 2D double-well) and reaching down to $\omega_n = 0.17$, and find that the first resonant tunneling in the transverse direction occurs at $\omega_n = 0.19$ and 0.18 for Ψ_G and Ψ_X, respectively. This resonant tunneling is achieved when the bosons tunnel from Ψ_G of the left well to $(y^2 - 1)\Psi_G$ of the right well. Similarly, for Ψ_X, the bosons tunnel from Ψ_X to $(y^2 - 1)\Psi_X$. The time evolution of the many-body survival

probability of Ψ_G and Ψ_X signifies that the rate of collapse of density oscillations is faster for Ψ_G compared to Ψ_X. This collapse of density oscillations occurs due to the growing degree of many-body correlations which is graphically shown in terms of the loss of coherence in the system.

To obtain further information of the time-dependent many-particle wavefunction, we present the many-particle variances of the observables, $\frac{1}{N}\Delta^2_{\hat{X}}(t)$, $\frac{1}{N}\Delta^2_{\hat{Y}}(t)$, $\frac{1}{N}\Delta^2_{\hat{P}_X}(t)$, $\frac{1}{N}\Delta^2_{\hat{P}_Y}(t)$, and $\frac{1}{N}\Delta^2_{\hat{L}_Z}(t)$, both at the longitudinal and transversal resonant tunneling conditions. Also, we demonstrate a possible interconnection of the above-mentioned quantities with the survival probability and loss of coherence. It is observed that the growing degree of fragmentation impacts the time-evolution of each variance for the longitudinal and transversal resonant tunneling differently. We notice that, in general, at the resonant tunneling, effects of breathing dynamics are amplified in the dynamics of variances. Focusing on the longitudinal resonant tunneling at $c = 0.5$, a signature of partial revival is observed in the dynamics of $\frac{1}{N}\Delta^2_{\hat{X}}(t)$, $\frac{1}{N}\Delta^2_{\hat{P}_X}(t)$, and $\frac{1}{N}\Delta^2_{\hat{L}_Z}(t)$. Also, in the longitudinal resonant tunneling, $\frac{1}{N}\Delta^2_{\hat{Y}}(t)$ shows a very small-amplitude fluctuations of the order of 10^{-3}, which is contrary to the transversal resonant tunneling where the amplitude of $\frac{1}{N}\Delta^2_{\hat{Y}}(t)$ is significantly high, of the order of 10^1. Moreover, the breathing oscillations in the dynamics of $\frac{1}{N}\Delta^2_{\hat{P}_Y}(t)$ at the longitudinal resonant tunneling is barely visible, while at the transversal resonant tunneling it is appreciable. Interestingly, at the transversal resonant tunneling, we notice a beating pattern in the dynamics of $\frac{1}{N}\Delta^2_{\hat{Y}}(t)$ and $\frac{1}{N}\Delta^2_{\hat{P}_Y}(t)$ which may arise due to the mixture of different breathing frequencies.

The present work can inspire several promising and interesting future research directions. An immediate extension would be the dynamics of even more intricate bosonic structures, e.g., vortex state or a mixture of vortex states induced by Raman process using light with orbital angular momentum [77–81] or by synthetic magnetic fields [82] in the longitudinal and transversal resonant tunneling conditions. Also, to apply a linear response theory [76] to accurately calculate the different breathing frequencies involved in the time evolution of different quantities at the resonant tunneling scenario would be challenging. Finally, in the long run we could envision that additional geometries would open up in three spatial dimensions.

APPENDIX A: MANY-PARTICLE VARIANCE

The variance of an observable, $\hat{A}$, is determined by the combination of the expectation values of $\hat{A}$ and $\hat{A}^2$. Here the expectation value of $\hat{A} = \sum_{j=1}^{N} \hat{a}(r_j)$ depends on the one-body operators while the expectation of $\hat{A}^2$ is a mixture of one- and two-body operators, $\hat{A}^2 = \sum_{j=1}^{N} \hat{a}^2(r_j) + \sum_{j<k} 2\hat{a}(r_j)\hat{a}(r_k)$. The variance can be written as [66]

$$\begin{aligned}\frac{1}{N}\Delta^2_{\hat{A}}(t) &= \frac{1}{N}[\langle\Psi(t)|\hat{A}^2|\Psi(t)\rangle - \langle\Psi(t)|\hat{A}|\Psi(t)\rangle^2] \\ &= \frac{1}{N}\Bigg\{\sum_j n_j(t)\int d\mathbf{r}\phi_j^*(\mathbf{r};t)\hat{a}^2(\mathbf{r})\phi_j(\mathbf{r};t) - \left[\sum_j n_j(t)\int d\mathbf{r}\phi_j^*(\mathbf{r};t)\hat{a}(\mathbf{r})\phi_j(\mathbf{r};t)\right]^2 \\ &+ \sum_{jpkq}\rho_{jpkq}(t)\left[\int d\mathbf{r}\phi_j^*(\mathbf{r};t)\hat{a}(\mathbf{r})\phi_k(\mathbf{r};t)\right]\left[\int d\mathbf{r}\phi_p^*(\mathbf{r};t)\hat{a}(\mathbf{r})\phi_q(\mathbf{r};t)\right]\Bigg\}, \end{aligned} \tag{A.1}$$

where $\{\phi_j(\mathbf{r};t)\}$ are the natural orbitals, $\{n_j(t)\}$ the natural occupations, and $\rho_{jpkq}(t)$ are the elements of the reduced two-particle density matrix, $\rho(\mathbf{r}_1,\mathbf{r}_2,\mathbf{r}_1',\mathbf{r}_2';t) = \sum_{jpkq}\rho_{jpkq}(t)\phi_j^*(\mathbf{r}_1';t)\phi_p^*(\mathbf{r}_2';t)$ $\phi_k(\mathbf{r}_1;t)\phi_q(\mathbf{r}_2;t)$. For one-body operators which are local in position space, the variance described in Eq A.1 boils down to [47]

$$\frac{1}{N}\Delta^2_{\hat{A}}(t) = \int d\mathbf{r}\frac{\rho(\mathbf{r};t)}{N}\hat{a}^2(\mathbf{r}) - N\left[\int\frac{\rho(\mathbf{r};t)}{N}\hat{a}(\mathbf{r})\right]^2 + \int d\mathbf{r}_1 d\mathbf{r}_2\frac{\rho^{(2)}(\mathbf{r}_1,\mathbf{r}_2,\mathbf{r}_1,\mathbf{r}_2;t)}{N}a(\mathbf{r}_1)a(\mathbf{r}_2), \tag{A.2}$$

where $\rho(\mathbf{r};t)$ is the time-dependent density. Eq A.1 describes the variances when the center-of-mass of the bosonic clouds are at the origin and the wavefunction is $\Psi(0,0)$ (or denoted in short by Ψ). As the initial states considered in this work are prepared at the position $(a,b) = (-2,0)$, here we present a general form of variances by incorporating the translated wavefunction, i.e., $\Psi(a,b)$ (or denoted in short by Ψ_{ab}). For the position and momentum operators, the variances do not change due to the translated wavefunction [66], therefore, $\frac{1}{N}\Delta^2_{\hat{X}}\Big|_{\Psi_{ab}} = \frac{1}{N}\Delta^2_{\hat{X}}\Big|_{\Psi}$, $\frac{1}{N}\Delta^2_{\hat{Y}}\Big|_{\Psi_{ab}} = \frac{1}{N}\Delta^2_{\hat{Y}}\Big|_{\Psi}$, $\frac{1}{N}\Delta^2_{\hat{P}_X}\Big|_{\Psi_{ab}} = \frac{1}{N}\Delta^2_{\hat{P}_X}\Big|_{\Psi}$, and $\frac{1}{N}\Delta^2_{\hat{P}_Y}\Big|_{\Psi_{ab}} = \frac{1}{N}\Delta^2_{\hat{P}_Y}\Big|_{\Psi}$. But, for the angular-momentum variance, the situation becomes intricate and expressed as [66]

$$\begin{aligned}\frac{1}{N}\Delta^2_{\hat{L}_Z}\Big|_{\Psi_{ab}} &= \frac{1}{N}\Delta^2_{\hat{L}_Z}\Big|_{\Psi} + \frac{1}{N}a^2\Delta^2_{\hat{P}_Y}\Big|_{\Psi} + \frac{1}{N}b^2\Delta^2_{\hat{P}_X}\Big|_{\Psi} \\ &+ \frac{1}{N}\Big\{a[\langle\Psi|\hat{L}_Z\hat{P}_Y + \hat{P}_Y\hat{L}_Z|\Psi\rangle - 2\langle\Psi|\hat{L}_Z|\Psi\rangle\langle|\Psi|\hat{P}_Y|\Psi\rangle] \\ &- b[\langle\Psi|\hat{L}_Z\hat{P}_X + \hat{P}_X\hat{L}_Z|\Psi\rangle - 2\langle\Psi|\hat{L}_Z|\Psi\rangle\langle|\Psi|\hat{P}_X|\Psi\rangle] \\ &- 2ab[\langle\Psi|\hat{P}_Y\hat{P}_X|\Psi\rangle - \langle\Psi|\hat{P}_Y|\Psi\rangle\langle|\Psi|\hat{P}_X|\Psi\rangle]\Big\}. \end{aligned} \tag{A.3}$$

Eq. (A.3) is used in the main text to evaluate the angular-momentum variance of the different initial conditions. For a wavefunction Ψ with particular spatial symmetry the evaluation of (A.3) can simplify.

APPENDIX B: ROLE OF THE WIDTH OF INTERPARTICLE INTERACTION POTENTIAL ON THE DYNAMICS

We have presented an extensive investigation leading to be a wealth of results on the physics of longitudinal and transversal resonant tunneling of a many-particle system in two spatial dimensions, both at the mean-field and many-body levels of theory. We have used a model potential of finite width and find it instructive and important to demonstrate the robustness of our findings to this parameter. In order to verify whether the width of the interparticle interaction potential, σ, affects the dynamical behavior at the longitudinal and transversal resonant conditions, we recomputed all the properties discussed in this work for two additional smaller widths, $\sigma = 0.25/\sqrt{\pi}$ and $\sigma = 0.25$, both at the mean-field and many-body levels. It is noted that the main text explores the dynamics with $\sigma = 0.25\sqrt{\pi}$ at both the resonant tunneling scenarios. In the mean-field dynamics, we find that the dynamical behavior of all the properties obtained for $\sigma = 0.25/\sqrt{\pi}$ and $\sigma = 0.25$ fall on top of the corresponding results computed for $\sigma = 0.25\sqrt{\pi}$. As for an example, we plot the dynamics of a sensitive quantity, $\frac{1}{N}\Delta^2_{\hat{X}}(t)$, see Fig. B1. The results for both resonant scenarios manifest that all the mean-field quantities discussed in this work are independent of σ.

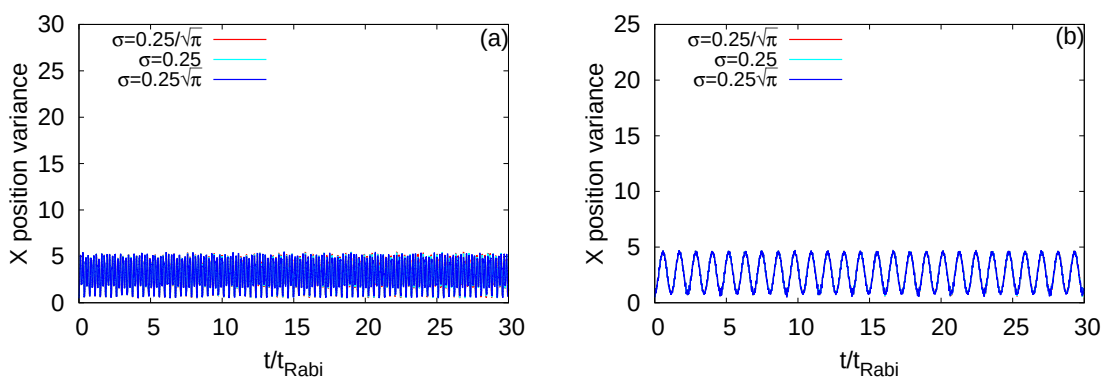

FIG. B1. Time-dependent mean-field position variance per particle along the x-direction, $\frac{1}{N}\Delta^2_{\hat{X}}(t)$, for the ground state at the (a) longitudinal ($c = 0.25$) and (b) transversal ($\omega_n = 0.19$) resonant scenarios. The three different widths of interparticle interaction potential are $\sigma = 0.25/\sqrt{\pi}$, $\sigma = 0.25$, and $\sigma = 0.25\sqrt{\pi}$. The interaction parameter is $\Lambda = 0.01\pi$. The mean-field results are found to be independent on σ. We show here dimensionless quantities. Color codes are explained in each panel.

To present the role of width of σ at the many-body dynamics, we select the dynamical behavior of the most sensitive quantities of the ground state at the first longitudinal resonant condition ($c = 0.25$) and transversal resonant condition ($\omega_n = 0.19$).

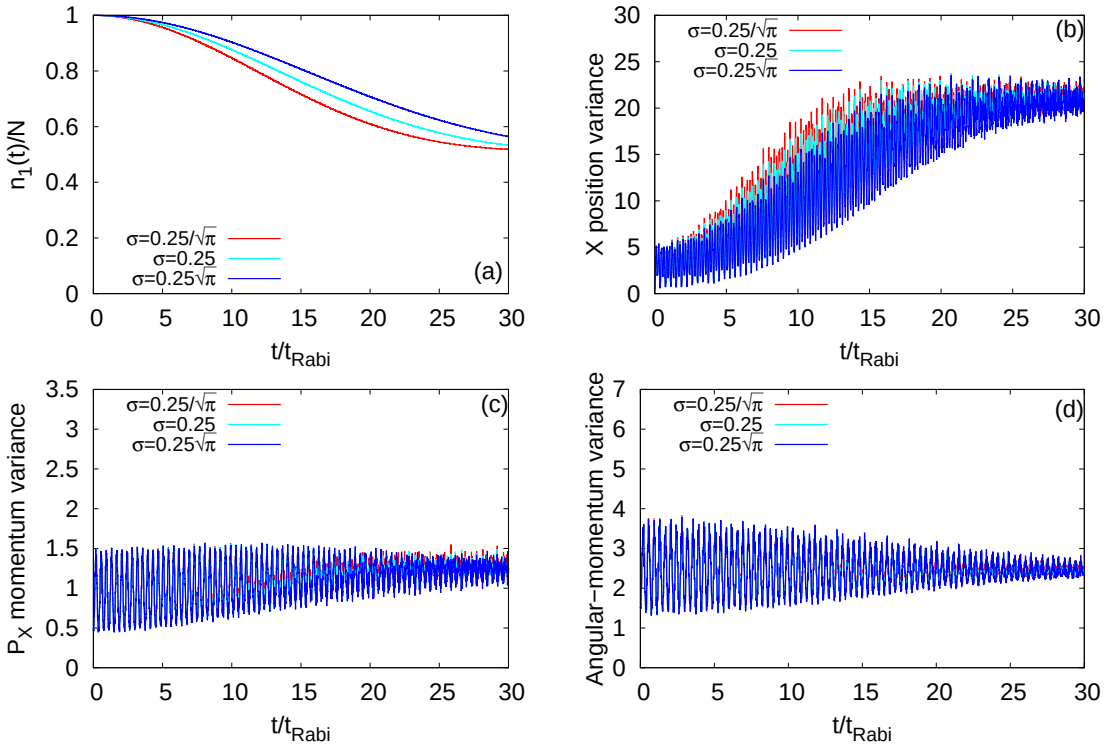

FIG. B2. Dependency of the many-body dynamics of ground state at the longitudinal resonant condition, $c = 0.25$, for the three different widths of interparticle interaction potential, i.e., $\sigma = 0.25/\sqrt{\pi}$, $\sigma = 0.25$, and $\sigma = 0.25\sqrt{\pi}$. The dynamics is shown by (a) $\frac{n_1(t)}{N}$, (b) $\frac{1}{N}\Delta^2_{\hat{X}}(t)$, (c) $\frac{1}{N}\Delta^2_{\hat{P}_X}(t)$, and (d) $\frac{1}{N}\Delta^2_{\hat{L}_Z}(t)$. The dynamics are computed with $N = 10$ bosons and the interaction parameter $\Lambda = 0.01\pi$. The many-body dynamics are computed with $M = 6$ time-dependent orbitals. The quantitative many-body results are found to be weakly dependent on σ. with We show here dimensionless quantities. Color codes are explained in each panel.

In Fig. B2, we present the many-body dynamics of $\frac{n_1(t)}{N}$, $\frac{1}{N}\Delta^2_{\hat{X}}(t)$, $\frac{1}{N}\Delta^2_{\hat{P}_X}(t)$, and $\frac{1}{N}\Delta^2_{\hat{L}_Z}(t)$ at $c = 0.25$. From Fig. B2 (a), one can observe that the rate of loss of coherence is slightly faster for $\sigma = 0.25/\sqrt{\pi}$ compared to other values of σ. It is found that decreasing the width of σ of the interparticle interaction potential gradually diminishes the quantitative difference between the dynamical behaviors of a particular quantity. Interestingly, the variances which are known to be sensitive many-body quantities due to depletion are hardly influenced by the width of σ. Although there is a small quantitative difference in the long-time fragmentation dynamics for the choices of σ, the many-body physics described for the longitudinal resonant scenario is robust which can be

seen in the dynamical behavior of the different quantum mechanical properties, see Fig. B2 (b), (c), and (d).

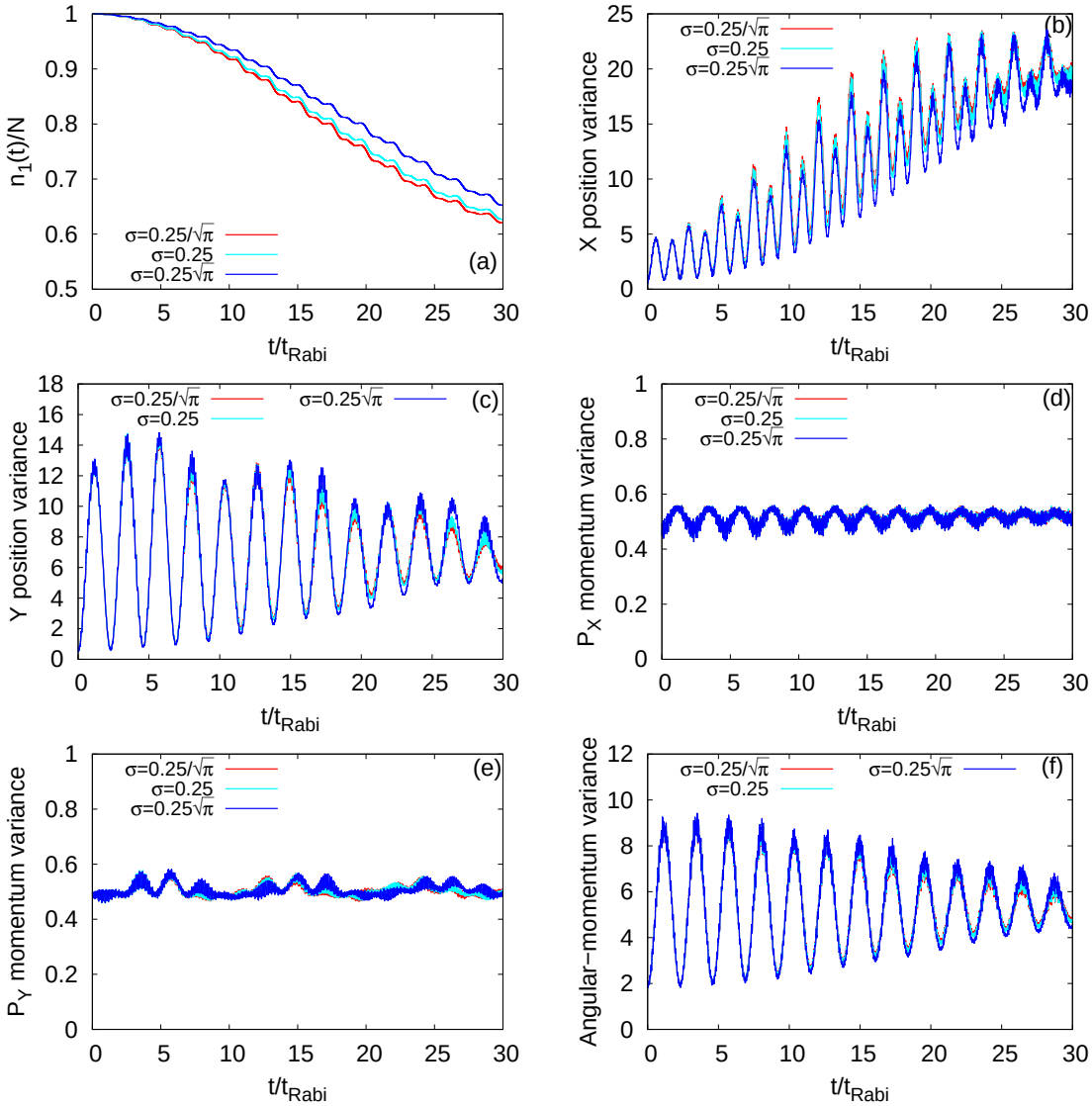

FIG. B3. Dependency of the many-body dynamics of ground state at the transversal resonant condition, $\omega_n = 0.19$, for the three different widths of interparticle interaction potential, i.e., $\sigma = 0.25/\sqrt{\pi}$, $\sigma = 0.25$, and $\sigma = 0.25\sqrt{\pi}$. The dynamics is shown by (a) $\frac{n_1(t)}{N}$, (b) $\frac{1}{N}\Delta^2_{\hat{X}}(t)$, (c) $\frac{1}{N}\Delta^2_{\hat{Y}}(t)$ (d) $\frac{1}{N}\Delta^2_{\hat{P}_X}(t)$, (e) $\frac{1}{N}\Delta^2_{\hat{P}_Y}(t)$, and (f) $\frac{1}{N}\Delta^2_{\hat{L}_Z}(t)$. The dynamics are computed with $N = 10$ bosons and the interaction parameter $\Lambda = 0.01\pi$. The many-body dynamics are computed with $M = 6$ time-dependent orbitals. The quantitative many-body results are found to be weakly dependent on σ. We show here dimensionless quantities. Color codes are explained in each panel.

Fig. B3 displays the role of σ at the transversal resonant scenario of the ground state. Here we present the dynamics of $\frac{n_1(t)}{N}$, $\frac{1}{N}\Delta^2_{\hat{X}}(t)$, $\frac{1}{N}\Delta^2_{\hat{Y}}(t)$ $\frac{1}{N}\Delta^2_{\hat{P}_X}(t)$, $\frac{1}{N}\Delta^2_{\hat{P}_Y}(t)$, and $\frac{1}{N}\Delta^2_{\hat{L}_Z}(t)$. Similar to

the longitudinal resonant scenario, here also, we notice that the development of the fragmentation is slightly quicker for $\sigma = 0.25/\sqrt{\pi}$ and slightly slower for $\sigma = 0.25\sqrt{\pi}$. Moreover, there is no qualitative difference in the tunneling dynamics at the transversal resonant scenario for the different choices of σ. The beating pattern in the dynamics of $\frac{1}{N}\Delta^2_{\hat{P}_Y}(t)$ is also observed at $\sigma = 0.25/\sqrt{\pi}$ and $\sigma = 0.25$. All in all, we demonstrate and observe that the width of the interparticle interaction potential does not qualitatively affect the mean-field and many-body physics of the tunneling dynamics at the resonant tunneling scenario.

ACKNOWLEDGMENTS

This research was supported by the Israel Science Foundation (Grants No. 600/15 and 1516/19). AB acknowledges Sudip Kumar Haldar for some helpful discussions. Computation time on the High Performance Computing system Hive of the Faculty of Natural Sciences at University of Haifa, and the Hawk at the High Performance Computing Center Stuttgart (HLRS) is gratefully acknowledged.

[1] Razavy, M. Quantum Theory of Tunneling (World Scientific, Singapore) (2003).

[2] Gamow, G. On the quantum theory of the atomic nucleus. Z Phys **51**, 204 (1928).

[3] Vatasescu, M., Dulieu, O., Amiot. C., Comparat, D., Drag, C., Kokoouline, V., Masnou-Seeuws, F. & Pillet, P. Multichannel tunneling in the $Cs_2 0_g$ photoassociation spectrum. Phys. Rev. A **61**, 044701 (2000).

[4] Wagner, M. & Mizuta, H. Complex-energy analysis of intrinsic lifetimes of resonances in biased multiple quantum wells. Phys. Rev. B **48**, 14393 (1993).

[5] Glutsch, S. Nonresonant and resonant Zener tunneling. Phys. Rev. B **69**, 235317 (2004).

[6] Josephson, B. D. Possible new effects in superconductive tunnelling. Phys. Lett. **1**, 251 (1962).

[7] Davis, J. C. & Packard, R. E. Superfluid ^{3}He Josephson weak links. Rev. Mod. Phys. **74**, 741 (2002).

[8] Albiezet, M., Gati, R., Fölling, J., Hunsmann, S., Cristiani, M. & Oberthaler, M. K. Direct Observation of Tunneling and Nonlinear Self-Trapping in a Single Bosonic Josephson Junction. Phys. Rev. Lett. **95**, 010402 (2005).

[9] Gati, R. & Oberthaler, M. K. A bosonic Josephson junction. J. Phys. B: At. Mol. Opt. Phys. **40**, R61 (2007).

[10] Smerzi, A., Fantoni, S., Giovanazzi, S. & Shenoy, S. R. Quantum coherent atomic tunneling between two trapped Bose-Einstein condensates Phys. Rev. Lett. **79**, 4950 (1997).

[11] Morsch, O. & Oberthaler, M. Dynamics of Bose-Einstein condensates in optical lattices. Rev. Mod. Phys. **78**, 179 (2006).

[12] Lewenstein, M., Sanpera, A., Ahufinger, V., Damski, B., Sen(De), A. & Sen, U. Ultracold atomic gases in optical lattices: mimicking condensed matter physics and beyond. Adv. Phys. **56**, 243 (2007).

[13] Lewenstein, M., Sanpera, A. & Ahufinger, V. Ultracold Atoms in Optical Lattices: Simulating Quantum Many-Body Systems (Oxford: Oxford University Press) (2012).

[14] Salgueiro, A. N., de Toledo Piza, A. F. R., Lemos, G. B., Drumond, R., Nemes, M. C. & Weidemüller, M. Quantum dynamics of bosons in a double-well potential: Josephson oscillations, self-trapping and ultralong tunneling times. Eur. Phys. J. D **44**, 537 (2007).

[15] Liu, Y. & Zhang, Y. Two atoms in a double well: exact solution with a Bethe ansatz. Phys. Rev. A **91**, 053610 (2015).

[16] Burchinati, A., Fort, C. & Modugno, M. Josephson plasma oscillations and the Gross-Pitaevskii equation: bogoliubov approach versus two-mode model. Phys. Rev. A **95**, 023627 (2017).

[17] Grynberg, G. & Robilliard, C. Cold atoms in dissipative optical lattices. Phys. Rep. **355**, 335 (2001).

[18] Haldar, S. K. & Alon, O. E. Impact of the range of the interaction on the quantum dynamics of a bosonic Josephson junction. Chemical Physics **509**, 72 (2018).

[19] Sakmann, K., Streltsov, A. I., Alon, O. E. & Cederbaum, L. S. Exact Quantum Dynamics of a Bosonic Josephson Junction. Phys. Rev. Lett. **103**, 220601 (2009).

[20] Dobrzyniecki, J. & Sowiński, T. Exact dynamics of two ultra-cold bosons confined in a one-dimensional double-well potential. Eur. Phys. J. D **70**, 83 (2016).

[21] Dobrzyniecki, J., Li, X., Nielsen, A. E. B. & Sowiński, T. Effective three-body interactions for bosons in a double-well confinement. Phys. Rev. A **97**, 013609 (2018).

[22] Vargas, J., Nuske, M., Eichberger, R., Hippler, C., Mathey, L. & Hemmerich, A. Orbital Many-Body Dynamics of Bosons in the Second Bloch Band of an Optical Lattice. Phys. Rev. Lett. **126**, 200402 (2021).

[23] Wirth, G., Ölschläger, M. & Hemmerich, A. Evidence for orbital superfluidity in the P-band of a bipartite optical square lattice. Nature Physics **7**, 147 (2011).

[24] Ölschläger, M., Wirth, G. & Hemmerich, A. Unconventional Superfluid Order in the F Band of a Bipartite Optical Square Lattice Phys. Rev. Lett. **106**, 015302 (2011).

[25] Bhowmik, A., Haldar, S. K. & Alon, O. E. Impact of the transverse direction on the many-body tunneling dynamics in a two-dimensional bosonic Josephson junction. Sci Rep **10**, 21476 (2020).

[26] Zenesini, A., Lignier, H., Tayebirad, G., Radogostowicz, J., Ciampini, D., Mannella, R., Wimberger, S., Morsch, O. & Arimondo, E. Time-resolved measurement of Landau-Zener tunneling in periodic potentials. Phys. Rev. Lett. **103**, 090403 (2009).

[27] Kolovsky, A. R. Topological phase transitions in tilted optical lattices. Phys. Rev. A **98**, 013603 (2018).

[28] Kolovsky, A. R. & Maksimov, D. N. Mott-insulator state of cold atoms in tilted optical lattices: doublon dynamics and multilevel Landau-Zener tunneling. Phys. Rev. A **94**, 043630 (2016).

[29] Kolovsky, A. R. Bright solitons and self-trapping with a Bose-Einstein condensate of atoms in driven tilted optical lattices. Phys. Rev. A **82**, 011601(R) (2010).

[30] Wilkinson, S. R., Bharucha, C. F., Madison, K. W., Niu, Q. & Raizen, M. G. Observation of Atomic Wannier-Stark Ladders in an Accelerating Optical Potential. Phys. Rev. Lett. **76**, 4512 (1996).

[31] Zenesini, A., Sias, C., Lignier, H., Singh, Y., Ciampini, D., Morsch, O., Mannella, R., Arimondo, E., Tomadin, A. & Wimberger, S. Resonant tunneling of Bose-Einstein condensates in optical lattices. New J. Phys. **10**, 053038 (2008).

[32] Sias, C., Zenesini, A., Lignier, H., Wimberger, S., Ciampini, D., Morsch, O. & Arimondo, E. Resonantly enhanced tunneling of Bose-Einstein condensates in periodic potentials. Phys. Rev. Lett. **98**, 120403 (2007).

[33] Greiner, M., Mandel, O., Esslinger, T., Hänsch, T. W. & Bloch, I. Nature **415**, 39 (2002).

[34] Lee, C., Fu, L. B. & Kivshar, Y. S. Many-body quantum coherence and interaction blockade in Josephson-linked Bose-Einstein condensates. Europhys. Lett. **81**, 60006 (2008).

[35] Rosam, B., Leo, K., Glück, M., Keck, F., Korsch, H. J., Zimmer, F. & Köhler, K. Lifetime of Wannier-Stark states in semiconductor superlattices under strong Zener tunneling to above-barrier bands, Phys. Rev. B **68**, 125301 (2003).

[36] Teo, B. K., Guest, J. R. & Raithel, G. Tunneling Resonances and Coherence in an Optical Lattice. Phys. Rev. Lett. **88**, 173001 (2002).

[37] Tsu, R. & Esaki, L. Tunneling in a finite superlattice. Appl. Phys. Lett. **22**, 562 (1973).

[38] Leo, K. High-Field Transport in Semiconductor Superlattices (Springer Verlag, Berlin, 2003)

[39] Haldar, S. K. & Alon, O. E. Many-body quantum dynamics of an asymmetric bosonic Josephson junction. New J. Phys. **21**, 103037 (2019).

[40] Landau, L. A Theory of Energy Transfer on Collisions. Phys. Z. Sowjetunion **1**, 88 (1932).

[41] Landau, L., A Theory of Energy Transfer II. Phys. Z. Sowjetunion **2**, 46 (1932).

[42] Zener, C., Non-adiabatic crossing of energy levels. Proc. R. Soc. A **137**, 696 (1932).

[43] Morsch, O., Müller, J. H., Cristiani, M., Ciampini, D. & Arimondo, E. Bloch Oscillations and Mean-Field Effects of Bose-Einstein Condensates in 1D Optical Lattices. Phys. Rev. Lett. **87**, 140402 (2001).

[44] Bharucha, C. F., Madison, K. W., Morrow, P. R., Wilkinson, S. R., Sundaram, B. & Raizen, M. G. Observation of atomic tunneling from an accelerating optical potential. Phys. Rev. A **55**, R857 (1997).

[45] Streltsov, A. I., Alon, O. E. & Cederbaum, L. S. Role of excited states in the splitting of a trapped interacting Bose-Einstein condensate by a time-dependent barrier. Phys. Rev. Lett. **99**, 030402 (2007).

[46] Alon, O. E., Streltsov, A. I. & Cederbaum, L. S. Multiconfigurational time-dependent Hartree method for bosons: many-body dynamics of bosonic systems. Phys. Rev. A **77**, 033613 (2008).

[47] Lode, A. U. J., Lévêque, C., Madsen, L. B., Streltsov, A. I. & Alon, O. E. Colloquium: Multiconfigurational time-dependent Hartree approaches for indistinguishable particles. Rev. Mod. Phys. **92**, 011001 (2020).

[48] Klaiman, S., & Alon, O. E. Variance as a sensitive probe of correlations. Phys. Rev. A **91**, 063613 (2015).

[49] Doganov, R. A., Klaiman, S., Alon, O. E., Streltsov, A. I. & Cederbaum, L. S. Two trapped particles interacting by a finite-range two-body potential in two spatial dimensions. Phys. Rev. A **87**, 033631 (2013).

[50] Beinke, R., Klaiman, S., Cederbaum, L. S., Streltsov, A. I. & Alon, O. E. Many-body tunneling dynamics of Bose-Einstein condensates and vortex states in two spatial dimensions. Phys. Rev. A **92**, 043627 (2015).

[51] Grond, J., Schmiedmayer, J. & Hohenester, U. Optimizing number squeezing when splitting a mesoscopic condensate. Phys. Rev. A **79**, 021603(R) (2009).

[52] Grond, J., Betz, T., Hohenester, U., Mauser, N. J., Schmiedmayer, J. & Schumm, T. The Shapiro effect in atom chip-based bosonic Josephson junctions. New J. Phys. **13**, 065026 (2011).

[53] Streltsova, O. I., Alon, O. E., Cederbaum, L. S. & Streltsov, A. I. Generic regimes of quantum many-body dynamics of trapped bosonic systems with strong repulsive interactions. Phys. Rev. A **89**, 061602(R) (2014).

[54] Klaiman, S., Lode, A. U. J., Streltsov, A. I., Cederbaum, L. S. & Alon, O. E. Breaking the resilience of a two-dimensional Bose-Einstein condensate to fragmentation. Phys. Rev. A **90**, 043620 (2014).

[55] Fischer, U. R., Lode, A. U. J. & Chatterjee, B. Condensate fragmentation as a sensitive measure of the quantum many-body behavior of bosons with long-range interactions. Phys. Rev. A **91**, 063621 (2015).

[56] Tsatsos, M. C. & Lode, A. U. J. Resonances and dynamical fragmentation in a stirred Bose-Einstein condensate. J. Low Temp. Phys. **181**, 171 (2015).

[57] Schurer, J. M., Negretti, A. & Schmelcher, P. Capture dynamics of ultracold atoms in the presence of an impurity ion. New J. Phys. **17**, 083024 (2015).

[58] Lode, A. U. J. & Bruder, C. Dynamics of Hubbard Hamiltonians with the multiconfigurational time-dependent Hartree method for indistinguishable particles. Phys. Rev. A **94**, 013616 (2016).

[59] Weiner, S. E., Tsatsos, M. C., Cederbaum, L. S. & Lode, A. U. J. Phantom vortices: hidden angular momentum in ultracold dilute Bose-Einstein condensates. Sci Rep **7**, 40122 (2017).

[60] Lode, A. U. J. & Bruder, C. Fragmented superradiance of a Bose-Einstein condensate in an optical cavity. Phys. Rev. Lett. **118**, 013603 (2017).

[61] Lode, A. U. J., Diorico, F. S., Wu, R., Molignini, P., Papariello, L., Lin, R., Lévêque, C., Exl, L., Tsatsos, M. C., Chitra, R. & Mauser, N. J. Many-body physics in two-component Bose-Einstein condensates in a cavity: fragmented superradiance and polarization. New J. Phys. **20**, 055006 (2018).

[62] Klaiman, S., Beinke, R., Cederbaum, L. S., Streltsov, A. I. & Alon, O. E. Variance of an anisotropic Bose-Einstein condensate. Chemical Physics **509**, 45 (2018).

[63] Alon, O. E. & Cederbaum, L. S. Attractive Bose-Einstein condensates in anharmonic traps: Accurate numerical treatment and the intriguing physics of the variance. Chemical Physics **515**, 287 (2018).

[64] Chatterjee, B., Tsatsos, M. C. & Lode, A. U. J. Correlations of strongly interacting one-dimensional ultracold dipolar few-boson systems in optical lattices. New J. Phys. **21**, 033030 (2019).

[65] Alon, O. E. Condensates in annuli: dimensionality of the variance. Molecular Physics **117**, 2108 (2019).

[66] Alon, O. E. Analysis of a Trapped Bose-Einstein Condensate in Terms of Position, Momentum, and Angular-Momentum Variance. Symmetry **11**, 1344 (2019).

[67] Sakmann, K., Streltsov, A. I., Alon, O. E. & Cederbaum, L. S. Quantum dynamics of attractive versus repulsive bosonic Josephson junctions: Bose-Hubbard and full-Hamiltonian results. Phys. Rev. A **82**, 013620 (2010).

[68] Sakmann, K., Streltsov, A. I., Alon, O. E. & Cederbaum, L. S. Universality of fragmentation in the Schrödinger dynamics of bosonic Josephson junctions. Phys. Rev. A **89**, 023602 (2014).

[69] Dalfovo, F., Giorgini, S., Pitaevskii, L. P. & Stringari, S. Theory of Bose-Einstein condensation in trapped gases. Rev. Mod. Phys. **71**, 463 (1999).

[70] Streltsov, A. I. & Streltsova, O. I. MCTDHB-Lab, Version 1. 5. 2015. Available online: (http://mctdhb-lab.com).

[71] Streltsov, A. I., Cederbaum, L. S., Alon, O. E., Sakmann, K., Lode, A. U. J., Grond, J., Streltsova, O. I., Klaiman, S. & Beinke, R. The Multiconfigurational Time-Dependent Hartree for Bosons Package, Version 3.x. Available online: http://mctdhb.org.

[72] Klaiman, S., Streltsov, A. I. & Alon, O. E. Uncertainty product of an out-of-equilibrium many-particle system. Phys. Rev. A **93**, 023605 (2016).

[73] Erdős, L., Schlein, B. & Yau, H. T. Rigorous Derivation of the Gross-Pitaevskii Equation. Phys. Rev. Lett. **98**, 040404 (2007).

[74] Coleman, A. J. & Yukalov, V. I. Reduced Density Matrices: Coulson's Challenge; Lectures Notes in Chemistry; Springer: Berlin, Germany, Volume 72 (2000).

[75] Sakmann, K., Streltsov, A. I., Alon, O. E. & Cederbaum, L. S. Reduced density matrices and coherence of trapped interacting bosons. Phys. Rev. A **78**, 023615 (2008).

[76] Theisen, M. & Streltsov, A. I. Many-body excitations and deexcitations in trapped ultracold bosonic clouds. Phys. Rev. A **94**, 053622 (2016).

[77] Schmiegelow, C. T., Schulz, J., Kaufmann, H., Ruster, T., Poschinger, U. G. & Schmidt-Kaler, F. Transfer of optical orbital angular momentum to a bound electron. Nature Communications **7**, 12998 (2016).

[78] Bhowmik, A., Mondal, P. K., Majumder, S. & Deb, B. Density profiles of two-component Bose-Einstein condensates interacting with a Laguerre-Gaussian beam. J. Phys. B: At. Mol. Opt. Phys. **51**, 135003 (2018).

[79] Bhowmik, A., Mondal, P. K., Majumder, S. & Deb, B. Interaction of atom with nonparaxial laguerre-gaussian beam: Forming superposition of vortex states in Bose-Einstein condensates. Phys. Rev. A **93**, 063852 (2016).

[80] Bhowmik, A. & Majumder, S. Tuning of non-paraxial effects of the Laguerre-Gaussian beam interacting with the two-component Bose-Einstein condensates. J. Phys. Commun. **2**, 125001 (2018).

[81] Bhowmik, A., Dutta, N. N. & Majumder, S. Vector polarizability of an atomic state induced by a linearly polarized vortex beam: External control of magic, tune-out wavelengths, and heteronuclear spin oscillations. Phys. Rev. A **102**, 063116 (2020).

[82] Price, R. M., Trypogeorgos, D., Campbell, D. L., Putra1, A., Valdés-Curiel, A. & Spielman, I. B. Vortex nucleation in a Bose-Einstein condensate: from the inside out. New J. Phys. **18**, 113009 (2016).

SUPPLEMENTAL MATERIAL FOR LONGITUDINAL AND TRANSVERSAL RESONANT TUNNELING OF INTERACTING BOSONS IN A TWO-DIMENSIONAL JOSEPHSON JUNCTION: MEAN-FIELD AND MANY-BODY DYNAMICS

In this supplemental material, we provide the convergences of the quantities discussed in the main text along with further complementary results and their analysis. The convergences of the results are shown with respect to the number of time-dependent orbitals and discrete-variable-representation grid points. The results are calculated by applying the multiconfigurational time-dependent Hartree for bosons (MCTDHB) method [1–3] and for our numerical computations, we use the numerical implementation in [4, 5]. We demonstrate the details of the mechanism of fragmentation in terms of the occupancy of the higher natural orbitals for both resonant tunneling conditions which were not discussed in the main text. Moreover, we graphically display the position and momentum variances [6, 7] along the y-direction for the longitudinal resonant tunneling at the mean-field and many-body levels (not shown in the main text). We have found in the main text that for Ψ_G and Ψ_X, the transversal resonant conditions are satisfied at $\omega_n = 0.19$ and $\omega_n = 0.18$, respectively, and demonstrated the variances only at the resonant values of ω_n. Here, we present all the many-body variances [8, 9], discussed in the main text, along with their convergences at $\omega_n = 0.18$, 0.19, and 0.20 for both the initial states. Some conclusions are drawn from the differences between the variances at and slightly off resonance. $M = 1$ represents the mean-field level. Here, the results are displayed for $M = 6$ and $M = 10$ time-dependent orbitals for Ψ_G and Ψ_X, and $M = 10$ and $M = 12$ time-dependent orbitals for Ψ_Y. The fully converged results imply that $M = 6$ time-dependent orbitals are required to accurately present the dynamics of Ψ_G and Ψ_X in the asymmetric 2D double-well potential, while for Ψ_Y, one requires $M = 10$ time-dependent orbitals for the time considered in this work [10]. It has been checked that the size of the 2D box considered in this work is adequate for both longitudinal and transversal scenarios. Section-V and section-VI describe the longitudinal and transversal resonant tunneling scenarios, respectively.

V. CONVERGENCES OF QUANTITIES IN LONGITUDINAL RESONANT TUNNELING

Here, the convergences of the many-body quantities in the longitudinal resonant tunneling condition are illustrated for the ground (Ψ_G) and transversely-excited (Ψ_Y) states. The computations performed in the main text are with $M = 6$ and 10 time-dependent orbitals for Ψ_G and Ψ_Y, respectively. Here, to testify the convergence with the orbital numbers, we repeat our computa-

tions with $M = 10$ and 12 time-dependent orbitals for Ψ_G and Ψ_Y, respectively. The bosonic clouds consist of $N = 10$ bosons with the interaction parameter $\Lambda = 0.01\pi$. Also, the many-body Hamiltonian is represented by 64×64 exponential discrete-variable-representation grid points in a box size $[-10, 10) \times [-10, 10)$. Here, we demonstrate the numerical convergences for the loss of coherence, fragmentation, and the variances of the position, momentum, and angular-momentum operators.

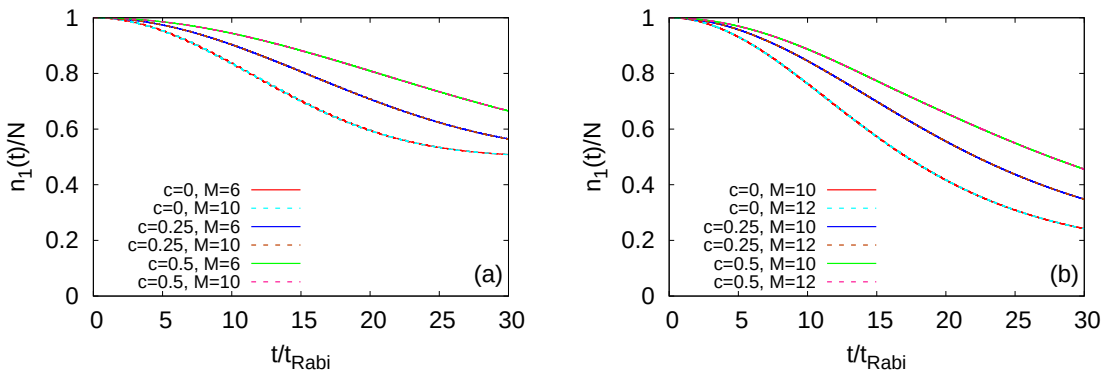

FIG. S1. Convergence of the occupation number per particle of the first natural orbital, $\frac{n_1(t)}{N}$, with the number of time-dependent orbitals for the initial states (a) Ψ_G and (b) Ψ_Y in the longitudinally-asymmetric 2D double-well potential. The bosonic clouds consist of $N = 10$ bosons with the interaction parameter $\Lambda = 0.01\pi$. The asymmetry parameters are $c = 0$, 0.25, and 0.5. The convergences is verified with $M = 6$, 10 time-dependent orbitals for the state Ψ_G. While we demonstrate the convergence of the results for Ψ_Y using $M = 10$, 12 time-dependent orbitals. We show here dimensionless quantities. Color codes are explained in each panel.

Fig. S1 represents the convergence of a basic quantity – loss of coherence – of the bosonic clouds, Ψ_G and Ψ_Y, in terms of the occupation numbers per particle of the first natural orbitals, $\frac{n_1(t)}{N}$. The figure showcases the results for all the asymmetry parameters, i.e., $c = 0$, 0.25, and 0.5, discussed in the main text. For both states, $\frac{n_1(t)}{N}$ decays with time with small background oscillations due to gradually increasing quantum correlations. The plots show that $\frac{n_1(t)}{N}$ computed from a larger number of time-dependent orbitals falls on top of the corresponding results calculated using a smaller number of time-dependent orbitals. The overlapping of the curves exhibits the convergence of $\frac{n_1(t)}{N}$ with the number of orbitals.

Having analyzed the convergence of $\frac{n_1(t)}{N}$, we investigate the further details of how the coherence is lost in the system by examining how fragmentation is developed. Fig. S2 displays the time evolution of the occupancies of the higher natural orbitals per particle, $\frac{n_{j>1}(t)}{N}$, for Ψ_G and Ψ_Y with their convergences with the number of time-dependent orbitals. Hence, convergence of the

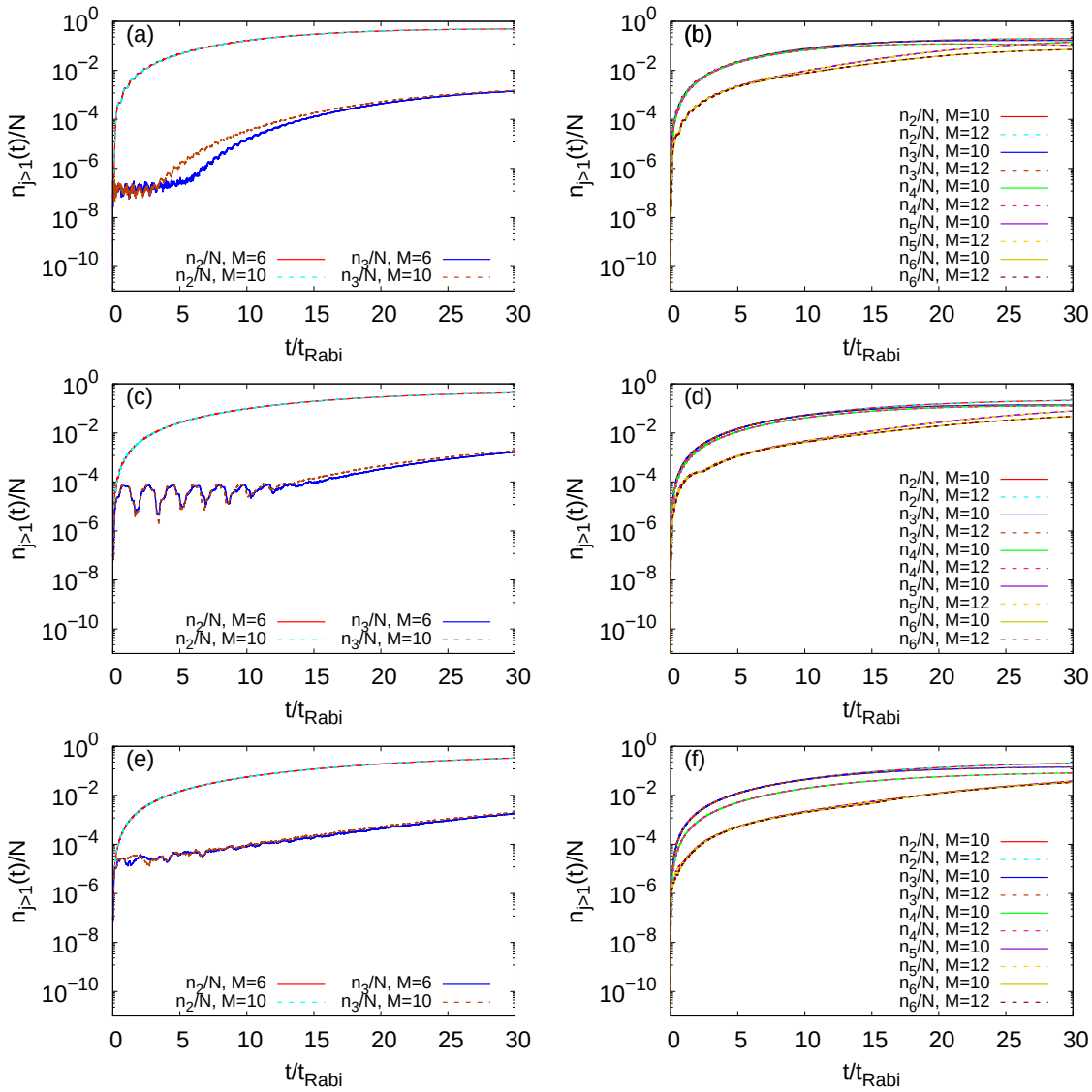

FIG. S2. Convergence of the natural occupation number per particle, $\frac{n_{j>1}(t)}{N}$, with the number of time-dependent orbitals for the initial states Ψ_G (left column) and Ψ_Y (right column) in the longitudinally-asymmetric 2D double-well potential. The bosonic clouds consist of $N = 10$ bosons with the interaction parameter $\Lambda = 0.01\pi$. The results for the asymmetry parameters $c = 0$, 0.25, and 0.5 are presented row-wise. The convergence is verified with $M = 6$, 10 time-dependent orbitals for the state Ψ_G. While we demonstrate the convergence of the results for Ψ_Y using $M = 10$, 12 time-dependent orbitals. We show here dimensionless quantities. Color codes are explained in each panel.

occupation numbers in the dynamics considered in this work is demonstrated from large to small (top to bottom).

As presented in the discussion of loss of coherence, here also, we plot $\frac{n_{j>1}(t)}{N}$ for the asymmetry parameters, $c = 0$, 0.25, and 0.5. The higher natural orbitals which have significant amount of

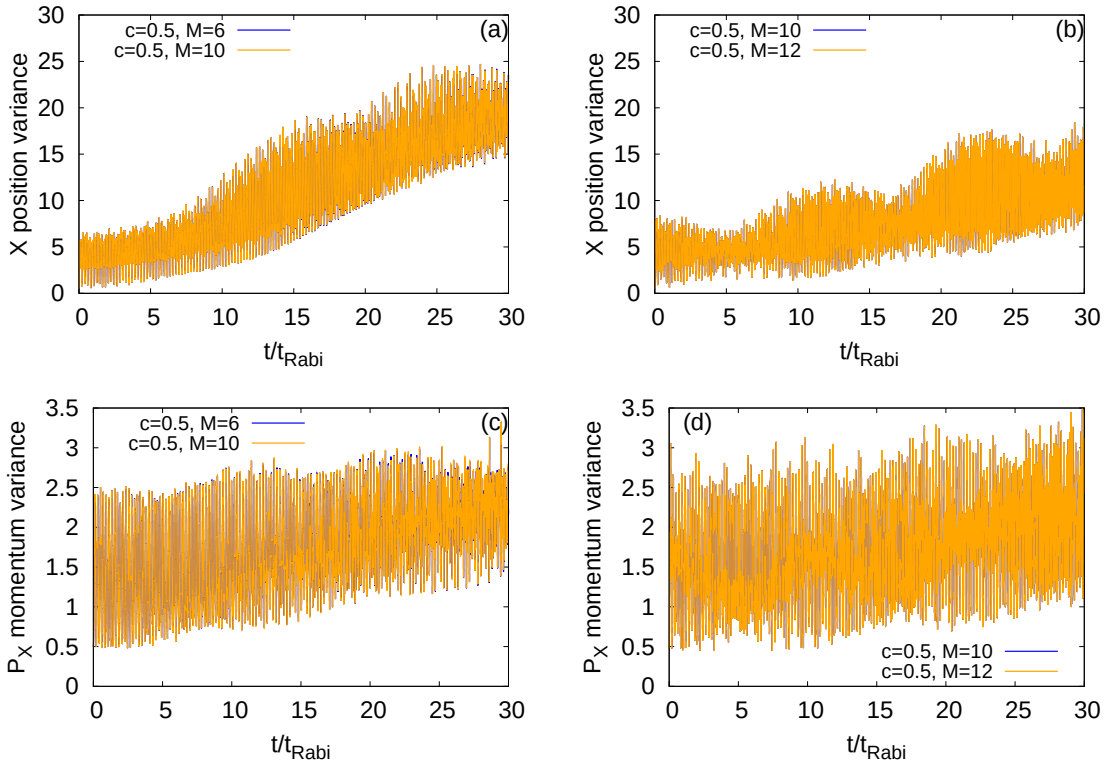

FIG. S3. Convergences of the time-dependent many-body position (1st row) and momentum (2nd row) variances per particle along the x-direction, $\frac{1}{N}\Delta^2_{\hat{X}}(t)$ and $\frac{1}{N}\Delta^2_{\hat{P}_X}(t)$, respectively, with the number of time-dependent orbitals for the initial states Ψ_G (left column) and Ψ_Y (right column) in the longitudinally-asymmetric 2D double-well potential. The bosonic clouds consist of $N = 10$ bosons with the interaction parameter $\Lambda = 0.01\pi$. The results are for the asymmetry parameter $c = 0.5$. The convergence is verified with $M = 6$, 10 time-dependent orbitals for the state Ψ_G. While we demonstrate the convergence of the results for Ψ_Y using $M = 10$, 12 time-dependent orbitals. We show here dimensionless quantities. Color codes are explained in each panel.

occupancies for Ψ_G (second and third natural orbitals) and Ψ_Y (second to sixth natural orbitals) are shown in the figure for all asymmetry parameters. To demonstrate the convergence with the time-dependent orbital numbers, we present the fragmentation dynamics with $M = 6$, 10 time-dependent orbitals for Ψ_G and $M = 10$, 12 time-dependent orbitals for Ψ_Y. Here it is observed that as time passes by the occupations of all the higher natural orbitals gradually increase (Note the logarithmic scale). Moreover, $\frac{n_3(t)}{N}$ of Ψ_G are oscillatory first and then increasing, clearly visible at $c = 0.25$. We notice that only two higher natural orbitals are considerably occupied for Ψ_G but for Ψ_Y, the amount of occupancies of the five higher natural orbitals are rather significant. The comparison of the fragmentation dynamics of Ψ_G and Ψ_Y exhibits that whenever the transverse excitations exist in the system, more natural orbitals are required to

accurately capture the dynamical behavior. However, the occupancies of the higher natural orbitals computed from a larger number of time-dependent orbitals overlap with the respective results found from a smaller number of time-dependent orbitals, indicating the convergence of the fragmentation dynamics for Ψ_G and Ψ_Y. The convergences of the occupancies of all the orbitals demonstrated till now automatically imply the convergence of the most basic quantity, i.e., survival probability, see Fig. 3 in the main text.

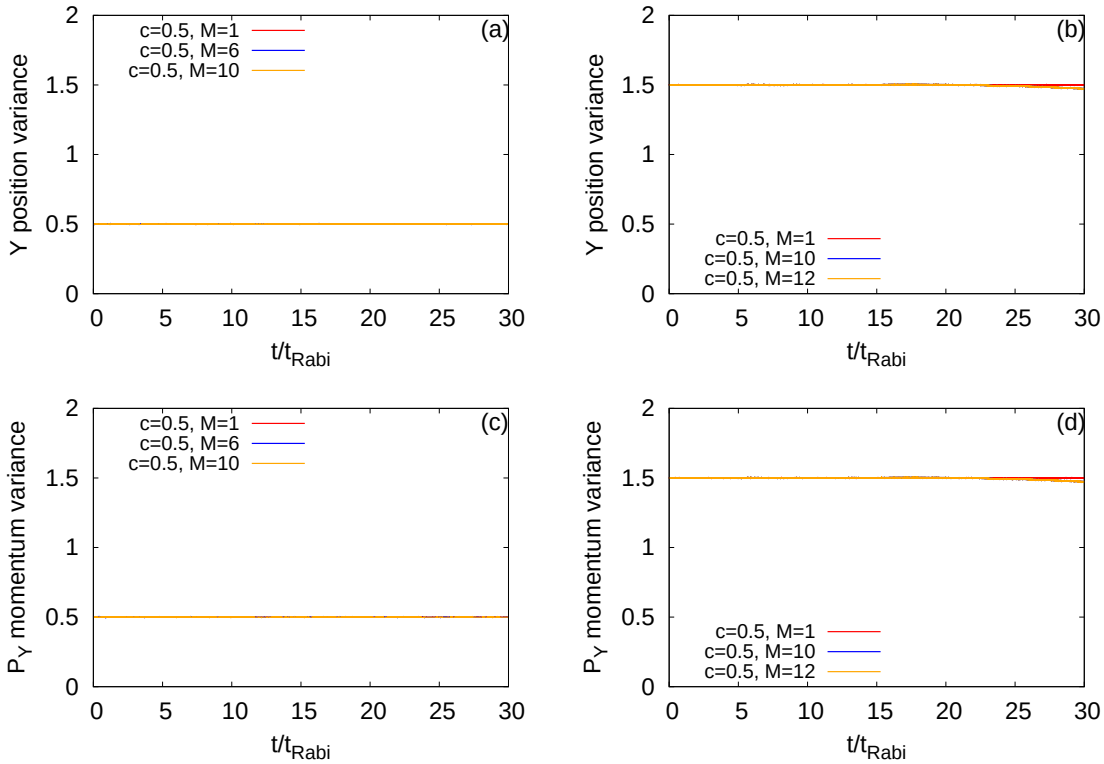

FIG. S4. Convergences of the time-dependent many-body position (1st row) and momentum (2nd row) variances per particle along the y-direction, $\frac{1}{N}\Delta^2_{\hat{Y}}(t)$ and $\frac{1}{N}\Delta^2_{\hat{P}_Y}(t)$, respectively, with the number of time-dependent orbitals for the initial states Ψ_G (left column) and Ψ_Y (right column) in the longitudinally-asymmetric 2D double-well potential. The bosonic clouds consist of $N = 10$ bosons with the interaction parameter $\Lambda = 0.01\pi$. The results are for the asymmetry parameter $c = 0.5$. $M = 1$ shows the mean-field results. The convergence is verified with $M = 6$, 10 time-dependent orbitals for the state Ψ_G. While we demonstrate the convergence of the results for Ψ_Y using $M = 10$, 12 time-dependent orbitals. We show here dimensionless quantities. Color codes are explained in each panel.

The time evolution of the many-body position and momentum variances per particle along the x-direction, $\frac{1}{N}\Delta^2_{\hat{X}}(t)$ and $\frac{1}{N}\Delta^2_{\hat{P}_X}(t)$, respectively, along with their numerical convergences with respect to the orbital numbers are illustrated in Fig. S3. Here, we checked and verified the convergences of $\frac{1}{N}\Delta^2_{\hat{X}}(t)$ and $\frac{1}{N}\Delta^2_{\hat{P}_X}(t)$ for all the asymmetry parameters discussed in the main

text. But, to demonstrate the convergence, we choose only the second resonant tunneling condition, i.e., $c = 0.5$. In the main text, we discussed that, at $c = 0.5$, $\frac{1}{N}\Delta^2_{\hat{X}}(t)$ and $\frac{1}{N}\Delta^2_{\hat{P}_X}(t)$ have two kinds of oscillations, namely, small frequency with large amplitude (due to the density oscillation) and high frequency with small amplitude (due to the breathing mode oscillation). The panels in Fig. S3 show that both variances are well converged with the orbital numbers. Even the oscillation which has high frequency with small amplitude, found with lower orbital numbers, overlaps with the corresponding results calculated from the higher orbital numbers.

As discussed in the main text, the many-particle position and momentum variances per particle along the y-direction, $\frac{1}{N}\Delta^2_{\hat{Y}}(t)$ and $\frac{1}{N}\Delta^2_{\hat{P}_Y}(t)$, respectively, have tiny fluctuations, of the order of 10^{-3} for all the asymmetry parameters discussed in this work. Here we graphically show the time evolution of $\frac{1}{N}\Delta^2_{\hat{Y}}(t)$ and $\frac{1}{N}\Delta^2_{\hat{P}_Y}(t)$ both at the mean-field and many-body levels along with their many-body convergences at $c = 0.5$, see Fig. S4. We observe that the almost frozen $\frac{1}{N}\Delta^2_{\hat{Y}}(t)$ and $\frac{1}{N}\Delta^2_{\hat{P}_Y}(t)$ for both states, Ψ_G and Ψ_Y, are fully converged with the number of orbitals.

Fig. S5 depicts the convergence of the many-body angular-momentum variance per particle, $\frac{1}{N}\Delta^2_{\hat{L}_Z}(t)$, for both initial states, Ψ_G and Ψ_Y. As mentioned in the dynamics of $\frac{1}{N}\Delta^2_{\hat{X}}(t)$ and $\frac{1}{N}\Delta^2_{\hat{P}_X}(t)$ at $c = 0.5$, here also, we observe the combined effect of the density and breathing-mode oscillations. There is no visible difference of $\frac{1}{N}\Delta^2_{\hat{L}_Z}(t)$ found when computed from the smaller and larger numbers of orbitals, which corresponds to the convergence of $\frac{1}{N}\Delta^2_{\hat{L}_Z}(t)$ with the number of orbitals.

Now, we demonstrate the convergence of the results described in the main text with the number of grid points. So far all the results for the longitudinal resonant tunneling scenario were computed with 64×64 grid points. To check the convergence with the grid points, we recomputed all the quantities with 128×128 grid points for all asymmetry parameters. In order to display the convergence of our results, we choose the most sensitive quantity, $\frac{1}{N}\Delta^2_{\hat{L}_Z}(t)$ presented in this work. We have verified that all quantities, the survival probability, occupation numbers, and the variances, $\frac{1}{N}\Delta^2_{\hat{X}}(t)$, $\frac{1}{N}\Delta^2_{\hat{Y}}(t)$ $\frac{1}{N}\Delta^2_{\hat{P}_X}(t)$, and $\frac{1}{N}\Delta^2_{\hat{P}_Y}(t)$, are fully converged with the grid density. The overlapping curves of $\frac{1}{N}\Delta^2_{\hat{L}_Z}(t)$ with increasing the grid density signifies that the results are fully converged for 64×64 grid points for all values of c for Ψ_G, and at $c = 0$ and 0.25 for Ψ_Y. The small difference at loner times in the results for the excited state in Fig. S6 (f) represents that $\frac{1}{N}\Delta^2_{\hat{L}_Z}(t)$ is well converged with 64×64 grid points at $c = 0.5$.

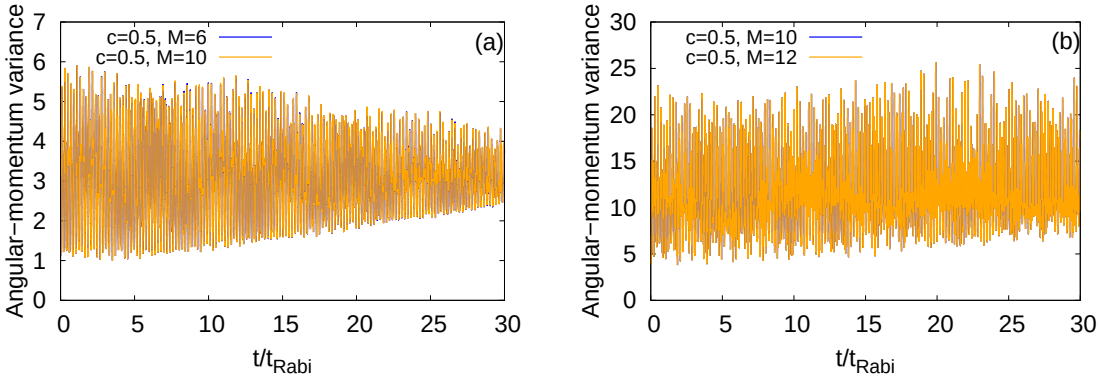

FIG. S5. Convergence of the time-dependent variance per particle of the z- component of the angular-momentum operator, $\frac{1}{N}\Delta^2_{\hat{L}_Z}(t)$, with the number of time-dependent orbitals for the initial states (a) Ψ_G and (b) Ψ_Y in the longitudinally-asymmetric 2D double-well potential. The bosonic clouds consist of $N = 10$ bosons with the interaction parameter $\Lambda = 0.01\pi$. The results are for the asymmetry parameter $c = 0.5$. The convergence is verified with $M = 6$, 10 time-dependent orbitals for the state Ψ_G. While we demonstrate the convergence of the results for Ψ_Y using $M = 10$, 12 time-dependent orbitals. We show here dimensionless quantities. Color codes are explained in each panel.

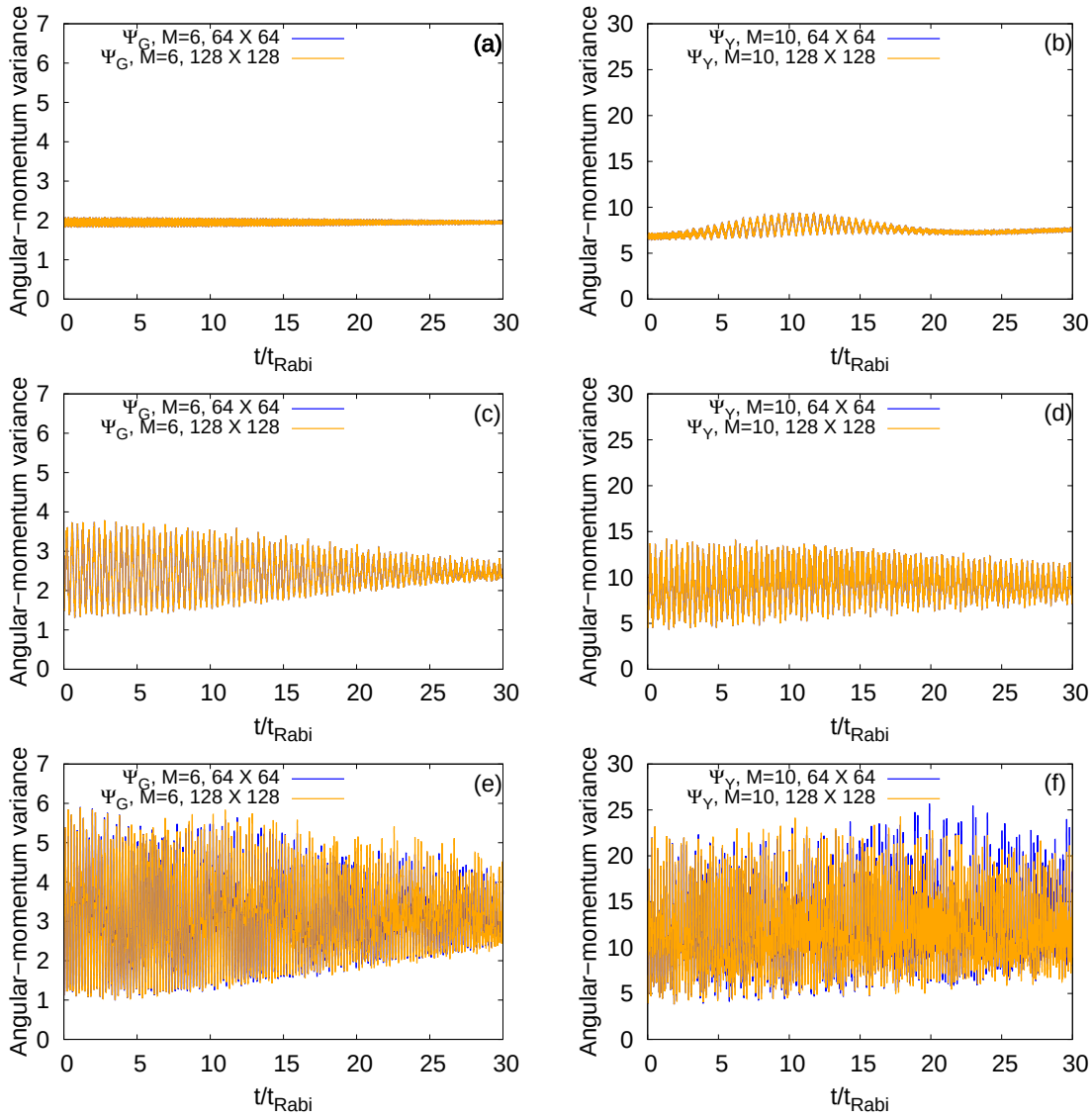

FIG. S6. Convergence of the time-dependent variance per particle of the z- component of the angular-momentum operator, $\frac{1}{N}\Delta^2_{\hat{L}_z}(t)$, with the number of grid points for the initial states Ψ_G (left column) and Ψ_Y (right column) in the longitudinally-asymmetric 2D double-well potential. The bosonic clouds consist of $N = 10$ bosons with the interaction parameter $\Lambda = 0.01\pi$. The results for the asymmetry parameters $c = 0$, 0.25, and 0.5 are presented row-wise. The convergence is verified with 64×64 and 128×128 grid points. We show here dimensionless quantities. Color codes are explained in each panel.

VI. CONVERGENCES OF QUANTITIES IN TRANSVERSAL RESONANT TUNNELING

Similar to the longitudinal resonant tunneling, now we demonstrate the convergence of the loss of coherence, fragmentation, and the variances of position, momentum, and angular-momentum operators with respect to the number of time-dependent orbitals and the density of the discrete-variable-representation grid points. Here, the initial states are Ψ_G and the longitudinally-excited state Ψ_X. In the main text, all the physical quantities in the transversal resonant tunneling for Ψ_G and Ψ_X are computed using $M = 6$ time-dependent orbitals. To verify the convergence with respect to the number of orbitals, we recomputed all the quantities with $M = 10$ time-dependent orbitals. For the transversal resonant tunneling, the many-body Hamiltonian is represented by 128×128 exponential discrete-variable-representation grid points in a box size of $[-10, 10) \times [-10, 10)$.

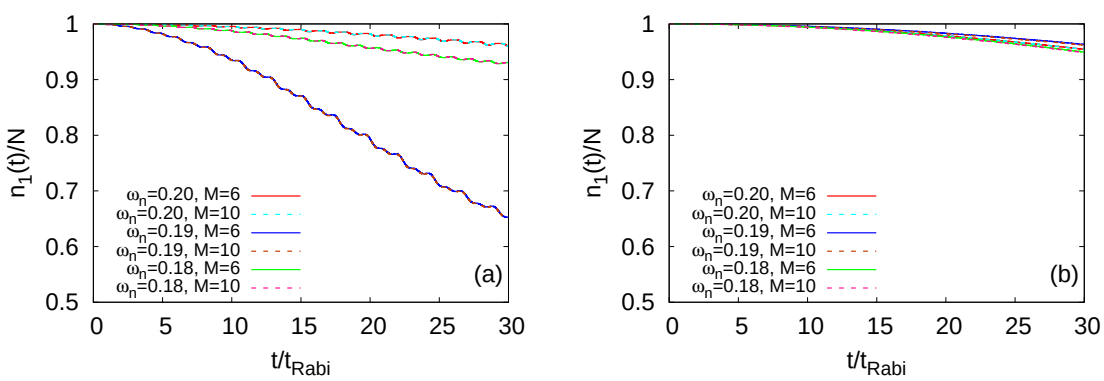

FIG. S7. Convergence of the occupation number per particle of the first natural orbital, $\frac{n_1(t)}{N}$, with the number of time-dependent orbitals for the initial states (a) Ψ_G and (b) Ψ_X in the transversely-asymmetric 2D double-well potential. The bosonic clouds consist of $N = 10$ bosons with the interaction parameter $\Lambda = 0.01\pi$. The frequencies are $\omega_n = 0.20$, 0.19, and 0.18. The convergence is verified with $M = 6$ and $M = 10$ time-dependent orbitals for both states. We show here dimensionless quantities. Color codes are explained in each panel.

Fig. S7 depicts the numerical convergence of the loss of coherence, represented as the occupation numbers per particle of the first natural orbital, $\frac{n_1(t)}{N}$, for Ψ_G and Ψ_X with the number of orbitals M. The frequency of the wider right well ω_n, see Eq.(2.5) and Fig. 1(b) of the main text, is considered as $\omega_n = 0.20$, 0.19, and 0.18. We remind that at $\omega_n = 0.19$ and 0.18, we find the transeversal resonant tunneling scenario for Ψ_G and Ψ_X, respectively. As discussed in the main text for $M = 6$ orbitals, here also for $M = 10$ orbitals, $\frac{n_1(t)}{N}$ decays with an oscillatory background for both initial states and falls on top of the corresponding results found from $M = 6$ orbitals,

indicating the convergence of condensate fraction with the number of orbitals.

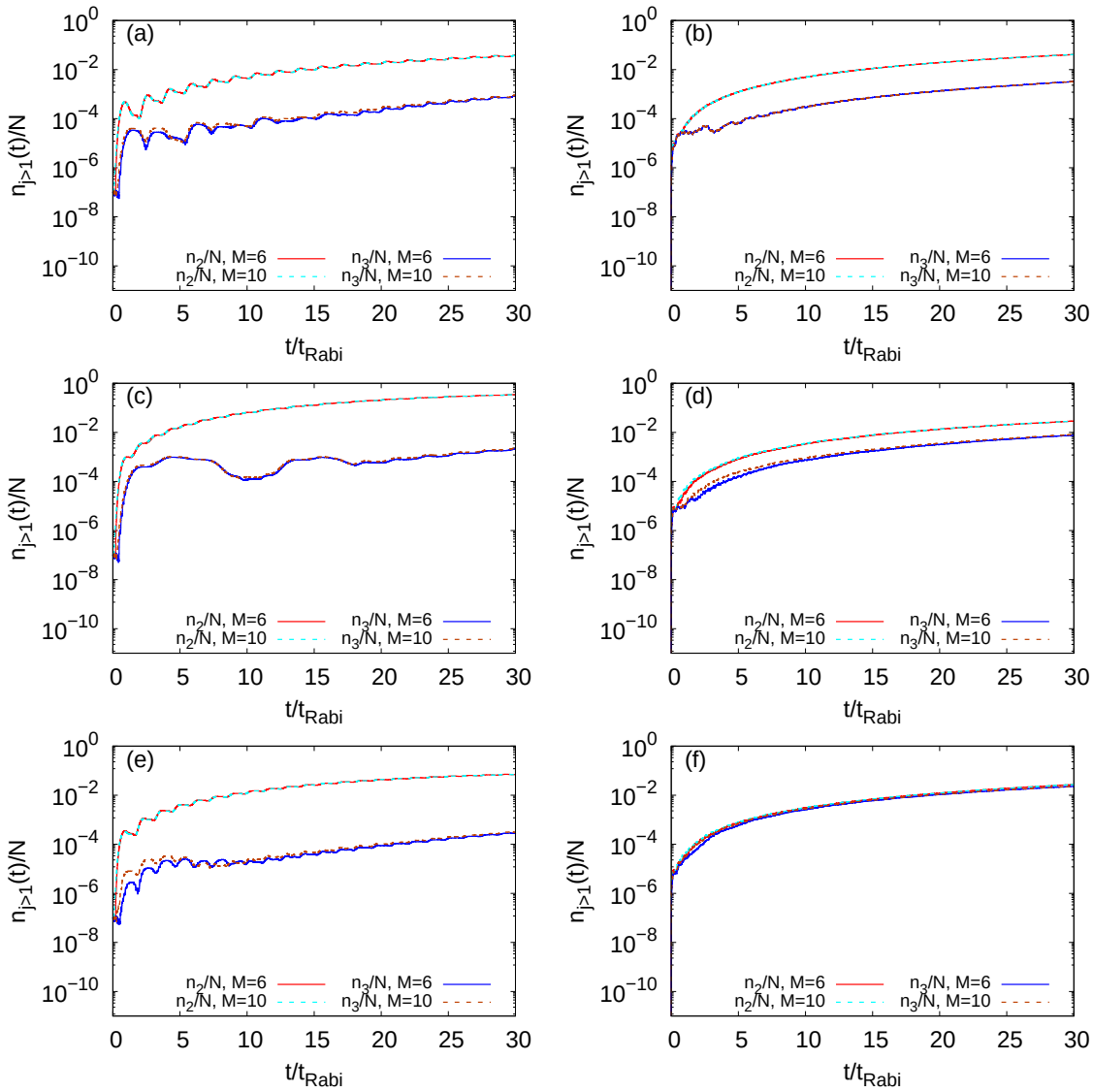

FIG. S8. Convergence of the natural occupation number per particle, $\frac{n_{j>1}(t)}{N}$, with the number of time-dependent orbitals for the initial states Ψ_G (left column) and Ψ_X (right column) in the transversely-asymmetric 2D double-well potential. The bosonic clouds consist of $N = 10$ bosons with the interaction parameter $\Lambda = 0.01\pi$. The results for the frequencies $\omega_n = 0.20$, 0.19, and 0.18 are presented row-wise. The convergence is verified with $M = 6$ and $M = 10$ time-dependent orbitals for both states. We show here dimensionless quantities. Color codes are explained in each panel.

In order to learn how the fragmentation develops in the transversal resonant tunneling scenario and at its vicinity, we explore the time-dependent occupancies of higher natural orbitals per particle, $\frac{n_{j>1}(t)}{N}$, along with their convergences with the number of orbitals for Ψ_G and Ψ_X. We graphically present only $\frac{n_2(t)}{N}$ and $\frac{n_3(t)}{N}$ in Fig. S8 as they have occupations in appreciable amount. Among

the three different values of ω_n, $\frac{n_2(t)}{N}$ is maximally occupied at $\omega_n = 0.19$ for Ψ_G and at $\omega_n = 0.18$ for Ψ_X, as these values of ω_n produce the transversal resonant tunneling for the respective states. We observe the oscillatory nature in the the dynamics of $\frac{n_2(t)}{N}$ and $\frac{n_3(t)}{N}$ for Ψ_G, whereas it is hardly visible for Ψ_X.

Figs. S9 and S10 show the many-body position and momentum variances per particle along the x-direction, $\frac{1}{N}\Delta^2_{\hat{X}}(t)$ and $\frac{1}{N}\Delta^2_{\hat{P}_X}(t)$, respectively, as well as their numerical convergences with number of orbitals. Here we analyze the many-body $\frac{1}{N}\Delta^2_{\hat{X}}(t)$ and $\frac{1}{N}\Delta^2_{\hat{P}_X}(t)$ at $\omega_n = 0.20$, 0.19, and 0.18 for both Ψ_G and Ψ_X. $\frac{1}{N}\Delta^2_{\hat{X}}(t)$ and $\frac{1}{N}\Delta^2_{\hat{P}_X}(t)$ computed with $M = 10$ orbitals fall on top of the corresponding quantities found from $M = 6$ orbitals, signifying the convergences of these quantities for both states. For Ψ_X, we observe marginal differences in terms of frequency and amplitude for both the quantities, $\frac{1}{N}\Delta^2_{\hat{X}}(t)$ and $\frac{1}{N}\Delta^2_{\hat{P}_X}(t)$, when computed at $\omega_n = 0.20$, 0.19, and 0.18. These marginal differences are consistent with the corresponding survival probabilities discussed in the main text. The differences are negligible for both the quantities at the three different frequencies for Ψ_X as it lies in the first excited band and feels a smaller barrier when it tunnels. The frequency of oscillations of $\frac{1}{N}\Delta^2_{\hat{X}}(t)$ for Ψ_X is practically half the corresponding oscillation frequency of the survival probabilities.

Unlike Ψ_X, we find significantly different many-body dynamics of $\frac{1}{N}\Delta^2_{\hat{X}}(t)$ and $\frac{1}{N}\Delta^2_{\hat{P}_X}(t)$ for Ψ_G at $\omega_n = 0.20$, 0.19, and 0.18. In order to characterize the nature of $\frac{1}{N}\Delta^2_{\hat{X}}(t)$ for Ψ_G, we notice that the average value of $\frac{1}{N}\Delta^2_{\hat{X}}(t)$ increases as time passes by, which is found to be maximal at the resonant value $\omega_n = 0.19$. As demonstrated for Ψ_G in the main text, the oscillation frequency of $\frac{1}{N}\Delta^2_{\hat{X}}(t)$ is twice the oscillation frequency of the survival probability at $\omega_n = 0.19$. Dissimilar to the resonant value of ω_n, here at $\omega_n = 0.18$ and 0.20, we find that the oscillation frequencies of the survival probability and $\frac{1}{N}\Delta^2_{\hat{X}}(t)$ practically overlap with each other. At $\omega_n = 0.19$, $\frac{1}{N}\Delta^2_{\hat{X}}(t)$ displays two different amplitudes of oscillations. This signature can also be seen at $\omega_n = 0.20$ (hardly visible). The time evolution of $\frac{1}{N}\Delta^2_{\hat{P}_X}(t)$ for Ψ_G is mostly dominated by the breathing mode oscillations. As time progresses, the amplitude of the oscillations of $\frac{1}{N}\Delta^2_{\hat{P}_X}(t)$ decreases for Ψ_G at all values of ω_n considered in this work.

In Figs. S11 and S12, we display the many-body position and momentum variances per particle along the y-direction, $\frac{1}{N}\Delta^2_{\hat{Y}}(t)$ and $\frac{1}{N}\Delta^2_{\hat{P}_Y}(t)$, respectively, for Ψ_G and Ψ_X at $\omega_n = 0.20$, 0.19, and 0.18, along with their numerical convergences with the number of orbitals. For both states, $\frac{1}{N}\Delta^2_{\hat{Y}}(t)$ and $\frac{1}{N}\Delta^2_{\hat{P}_Y}(t)$ computed using $M = 6$ and $M = 10$ time-dependent orbitals fall on top of each other, signifying the convergence of the quantities with the number of orbitals. For Ψ_G,

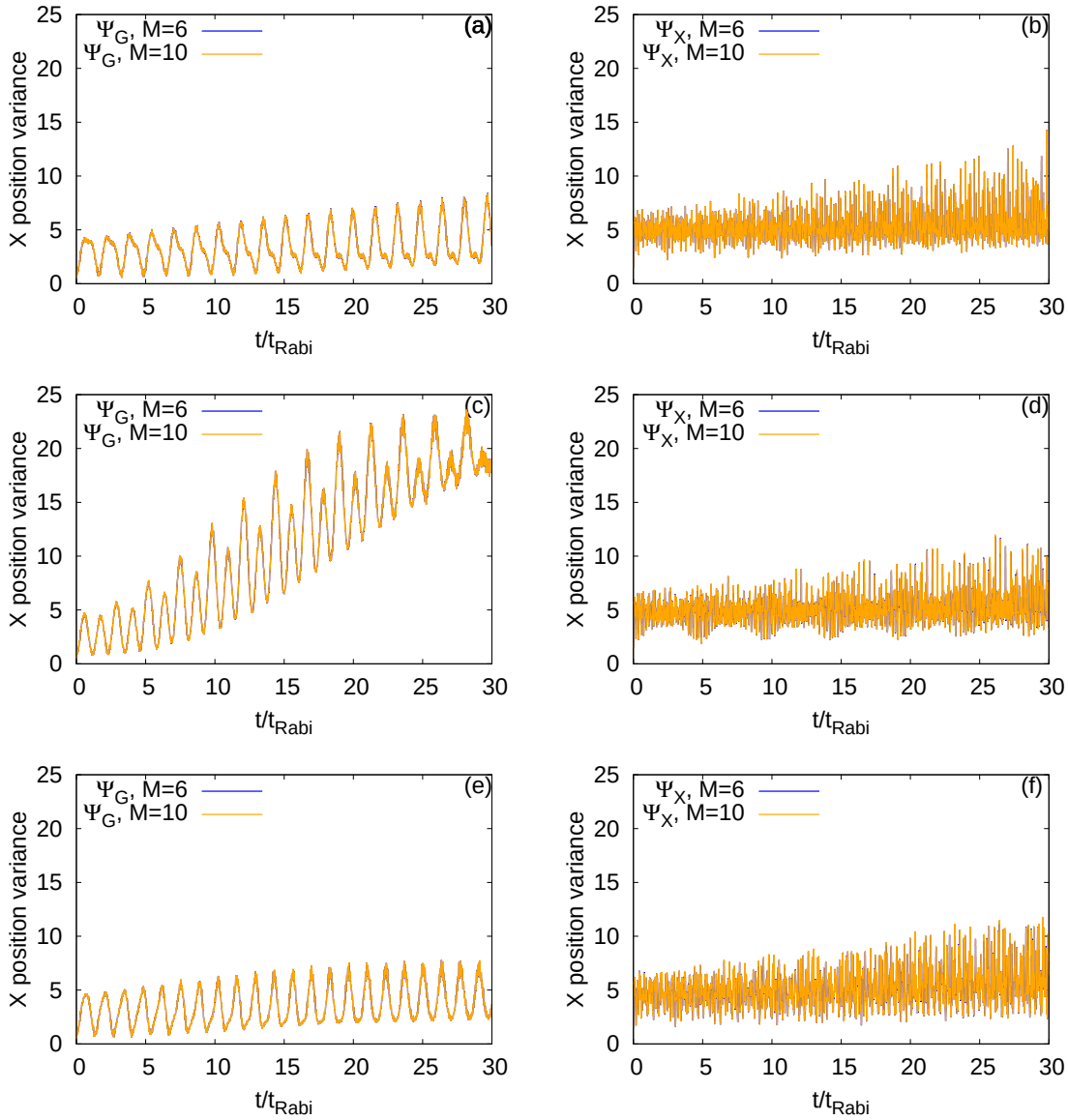

FIG. S9. Convergence of the time-dependent many-body position variance per particle along the x-direction, $\frac{1}{N}\Delta^2_{\hat{X}}(t)$, with the number of time-dependent orbitals for the initial states Ψ_G (left column) and Ψ_X (right column) in the transversely-asymmetric 2D double-well potential. The bosonic clouds consist of $N = 10$ bosons with the interaction parameter $\Lambda = 0.01\pi$. The results for the frequencies $\omega_n = 0.20$, 0.19, and 0.18 are presented row-wise. The many-body results are computed with $M = 6$ time-dependent orbitals. The convergence is verified with $M = 10$ time-dependent orbitals. We show here dimensionless quantities. Color codes are explained in each panel.

the amplitude of the many-body time evolution of $\frac{1}{N}\Delta^2_{\hat{Y}}(t)$ decays with the growing degree of correlations, see Fig. S11, and the decay rate is maximal at $\omega_n = 0.19$ and minimal at $\omega_n = 0.20$. At the resonant value for Ψ_G, $\omega_n = 0.19$, the amplitude of $\frac{1}{N}\Delta^2_{\hat{Y}}(t)$ reaches upto around 15, while

at the other frequencies they are comparatively small, i.e., around 4.5 at $\omega_n = 0.18$ and around 6.5 at $\omega_n = 0.20$. For the slower rate of growth of the fragmentation for Ψ_X in comparison to Ψ_G, the decay rate of the many-body $\frac{1}{N}\Delta^2_{\hat{Y}}(t)$ is hardly visible even at the resonant value of ω_n, see Fig. S11. By comparing the many-body $\frac{1}{N}\Delta^2_{\hat{Y}}(t)$ at different frequencies for Ψ_X, we observe that at the resonant condition for Ψ_X, i.e., $\omega_n = 0.18$, the amplitude of oscillation reaches upto 12 whereas at $\omega_n = 0.19$ and $\omega_n = 0.20$, the respective amplitudes reach upto around 10.5 and 9, respectively.

Focusing on the momentum variance along the y-direction for Ψ_G, we notice that at $\omega_n = 0.18$ and $\omega_n = 0.20$, $\frac{1}{N}\Delta^2_{\hat{P}_Y}(t)$ have the amplitudes of fluctuations of the order of 10^{-2} and at the resonant value the respective fluctuations of amplitude become 10^{-1}. In case of Ψ_X, the amplitude of fluctuations of $\frac{1}{N}\Delta^2_{\hat{P}_Y}(t)$ for Ψ_X is large compared to Ψ_G at each value of ω_n. We notice that the amplitude of $\frac{1}{N}\Delta^2_{\hat{P}_Y}(t)$ for Ψ_X fluctuates between approximately 0.23 to 0.60 at all three frequencies.

Fig. S13 collects the numerical convergence of the angular-momentum variance per particle, $\frac{1}{N}\Delta^2_{\hat{L}_Z}(t)$, for Ψ_G and Ψ_X at $\omega_n = 0.20$, 0.19, and 0.18. As discussed for $\frac{1}{N}\Delta^2_{\hat{Y}}(t)$, here also the amplitude of $\frac{1}{N}\Delta^2_{\hat{L}_Z}(t)$ decays with time for Ψ_G. The decay rate is the slowest at $\omega_n = 0.20$ and fastest at $\omega_n = 0.19$. But for Ψ_X, $\frac{1}{N}\Delta^2_{\hat{L}_Z}(t)$ does not follow the trend of a decaying amplitude as for Ψ_G. In general, we observe that at the resonant value of ω_n, $\frac{1}{N}\Delta^2_{\hat{L}_Z}(t)$ takes maximum value compared to other ω_n frequencies considered here. Moreover, comparing the many-body time evolution of $\frac{1}{N}\Delta^2_{\hat{L}_Z}(t)$, computed using $M = 6$ and 10 orbitals, signifies that the results are fully converged with $M = 6$ orbitals.

The main text and the supplemental material so far describe all quantities, i.e., the survival probability, loss of coherence, fragmentation, and the variances for the transversal resonant scenario with 128×128 grid points. In order to verify the convergence with the grid points, we repeat our computation with 256×256 grid points for both objects, Ψ_G and Ψ_X and of course the computations become demanding due to the increased grid density. To demonstrate the convergence with the grid points, we display $\frac{1}{N}\Delta^2_{\hat{L}_Z}(t)$ which is the most sensitive quantity discussed in this work. Fig. S14 displays the convergence of the many-body $\frac{1}{N}\Delta^2_{\hat{L}_Z}(t)$ at $\omega_n = 0.19$ for Ψ_G and $\omega_n = 0.18$ for Ψ_X, as there is no visible effect with increasing the number of grid points. Of course all other quantities are similarly converged.

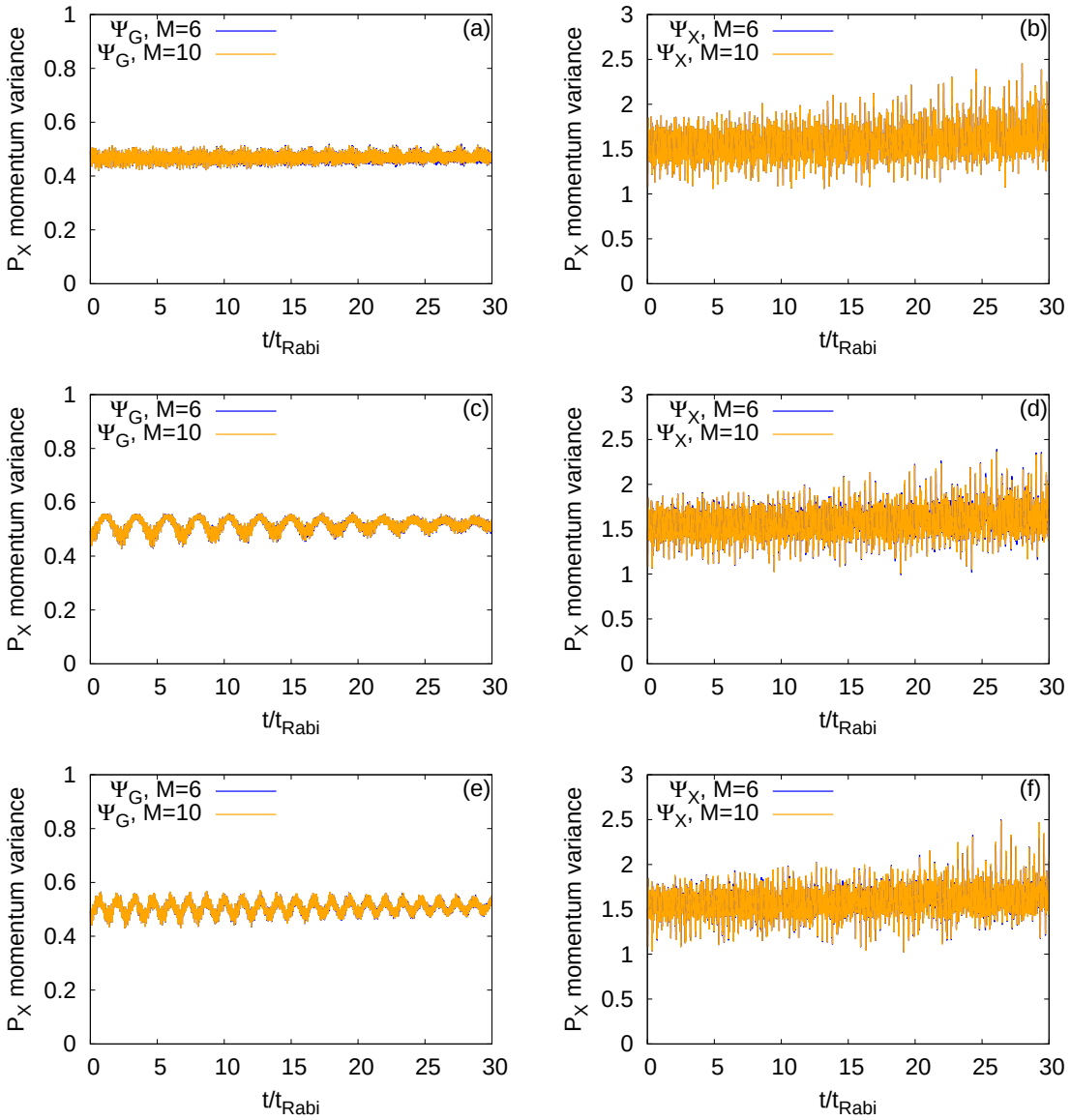

FIG. S10. Convergence of the time-dependent many-body momentum variance per particle along the x-direction, $\frac{1}{N}\Delta^2_{\hat{P}_X}(t)$, with the number of time-dependent orbitals for the initial states Ψ_G (left column) and Ψ_X (right column) in the transversely-asymmetric 2D double-well potential. The bosonic clouds consist of $N = 10$ bosons with the interaction parameter $\Lambda = 0.01\pi$. The results for the frequencies $\omega_n = 0.20$, 0.19, and 0.18 are presented row-wise. The many-body results are computed with $M = 6$ time-dependent orbitals. The convergence is verified with $M = 10$ time-dependent orbitals. We show here dimensionless quantities. Color codes are explained in each panel.

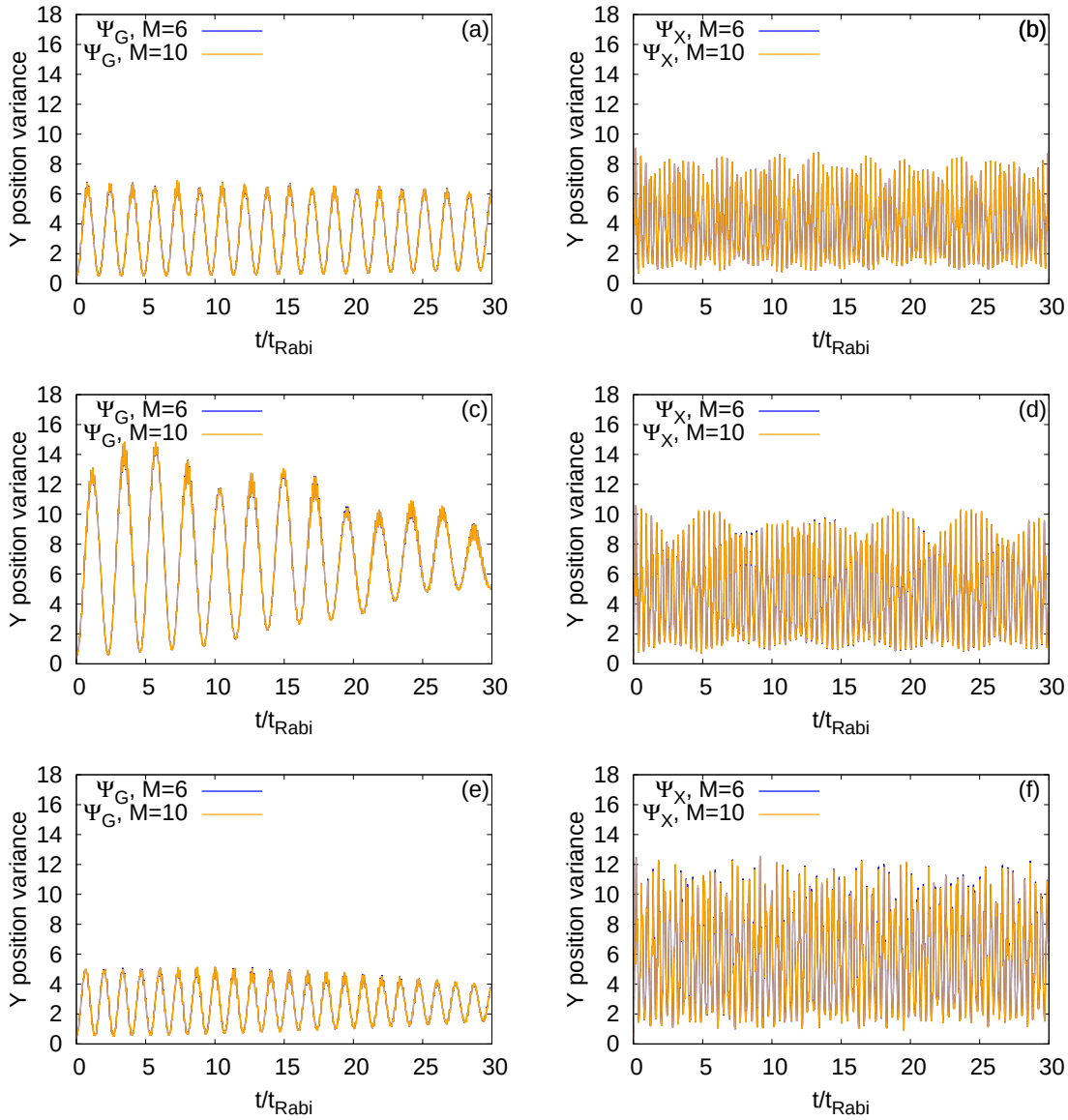

FIG. S11. Convergence of the time-dependent many-body position variance per particle along the y-direction, $\frac{1}{N}\Delta^2_{\hat{Y}}(t)$, with the number of time-dependent orbitals for the initial states Ψ_G (left column) and Ψ_X (right column) in the transversely-asymmetric 2D double-well potential. The bosonic clouds consist of $N = 10$ bosons with the interaction parameter $\Lambda = 0.01\pi$. The results for the frequencies $\omega_n = 0.20$, 0.19, and 0.18 are presented row-wise. The many-body results are computed with $M = 6$ time-dependent orbitals. The convergence is verified with $M = 10$ time-dependent orbitals. We show here dimensionless quantities. Color codes are explained in each panel.

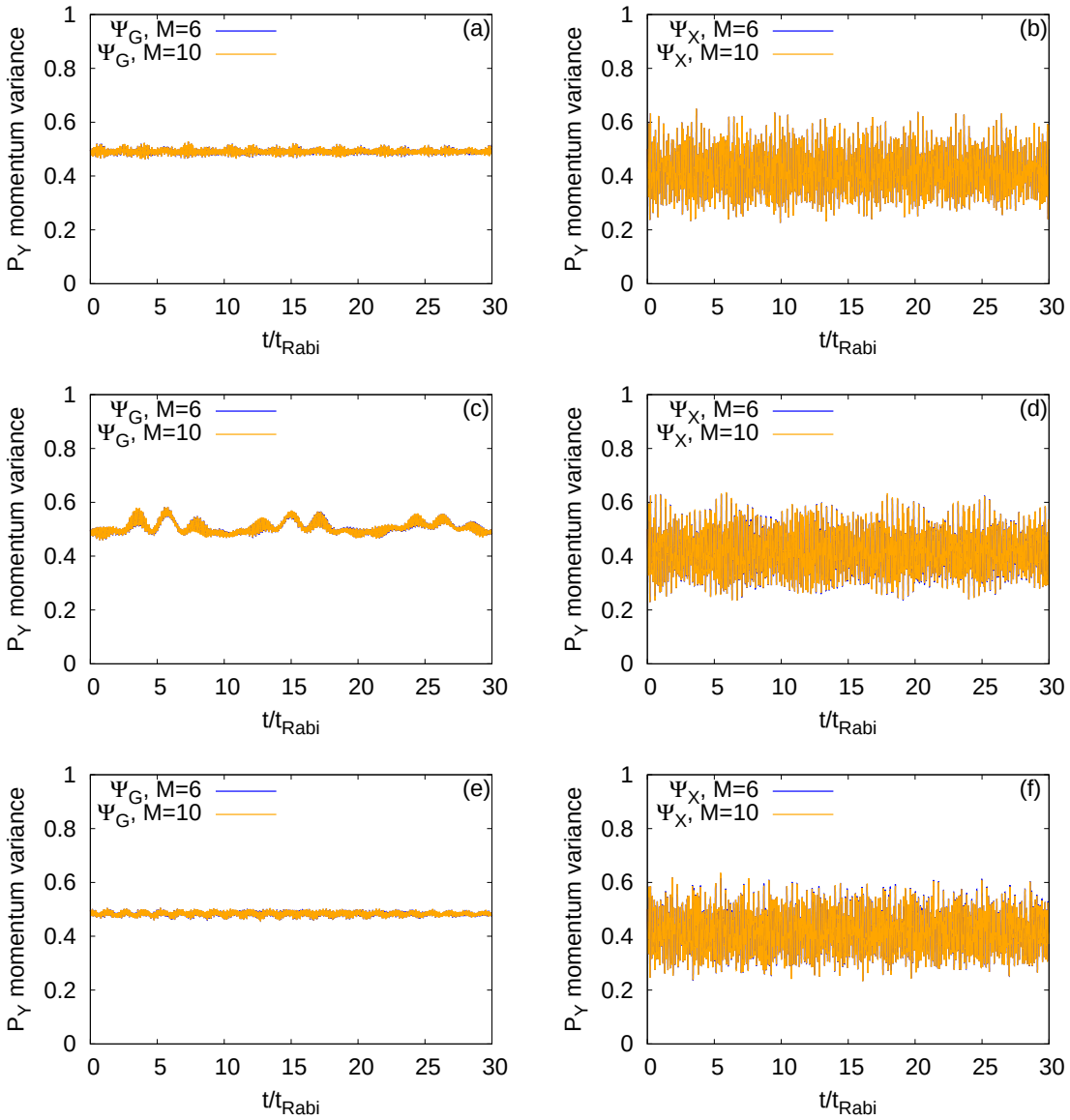

FIG. S12. Convergence of the time-dependent many-body momentum variance per particle along the y-direction, $\frac{1}{N}\Delta^2_{\hat{P}_Y}(t)$, with the number of time-dependent orbitals for the initial states Ψ_G (left column) and Ψ_X (right column) in the transversely-asymmetric 2D double-well potential. The bosonic clouds consist of $N = 10$ bosons with the interaction parameter $\Lambda = 0.01\pi$. The results for the frequencies $\omega_n = 0.20$, 0.19, and 0.18 are presented row-wise. The many-body results are computed with $M = 6$ time-dependent orbitals. The convergence is verified with $M = 10$ time-dependent orbitals. We show here dimensionless quantities. Color codes are explained in each panel.

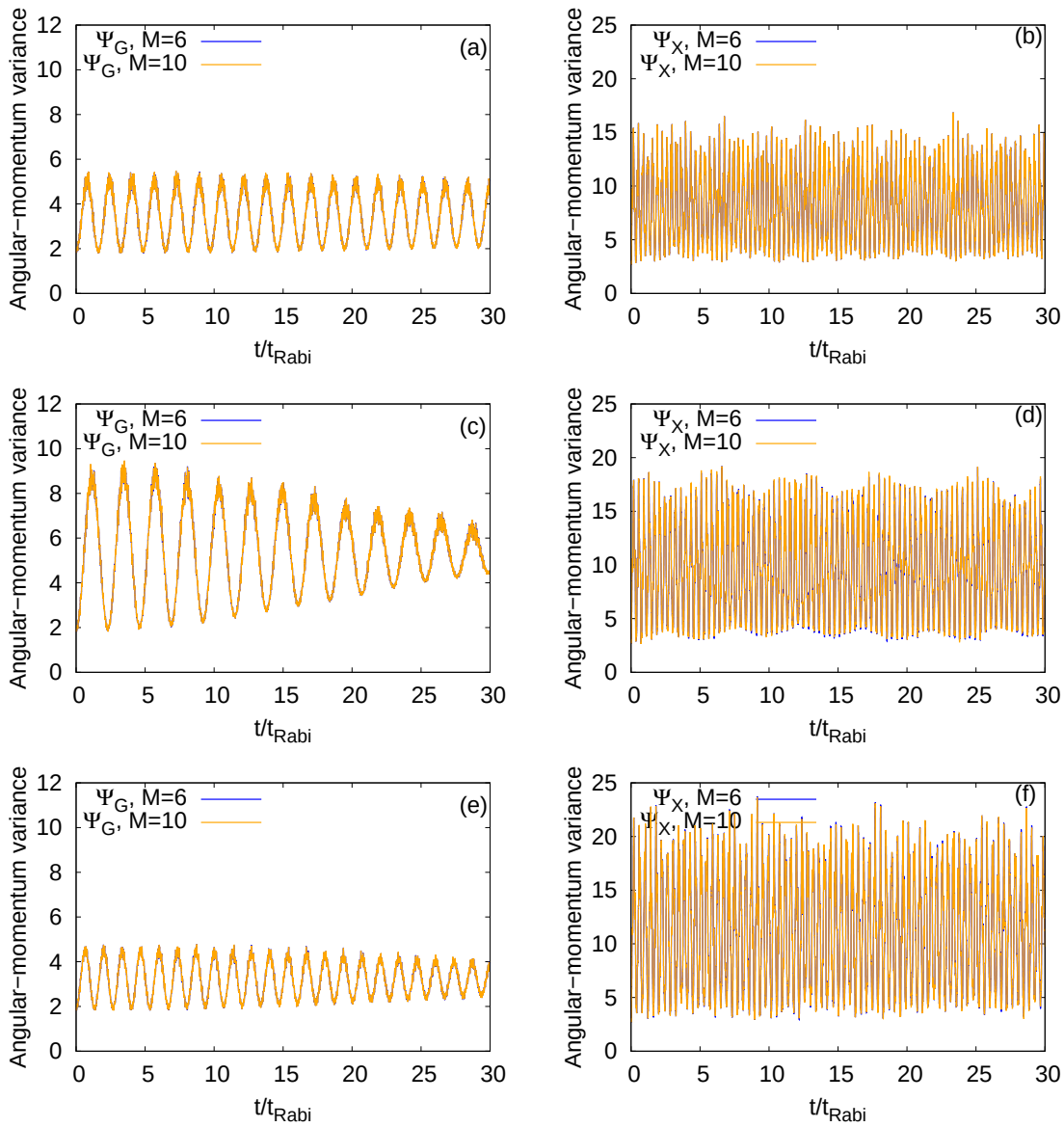

FIG. S13. Convergence of the time-dependent variance per particle of the z- component of the angular-momentum operator, $\frac{1}{N}\Delta^2_{\hat{L}_Z}(t)$, with the number of time-dependent orbitals for the initial states Ψ_G (left column) and Ψ_X (right column) in the transversely-asymmetric 2D double-well potential. The bosonic clouds consist of $N = 10$ bosons with the interaction parameter $\Lambda = 0.01\pi$. The results for the frequencies $\omega_n = 0.20$, 0.19, and 0.18 are presented row-wise. The many-body results are computed with $M = 6$ time-dependent orbitals. The convergence is verified with $M = 10$ time-dependent orbitals. We show here dimensionless quantities. Color codes are explained in each panel.

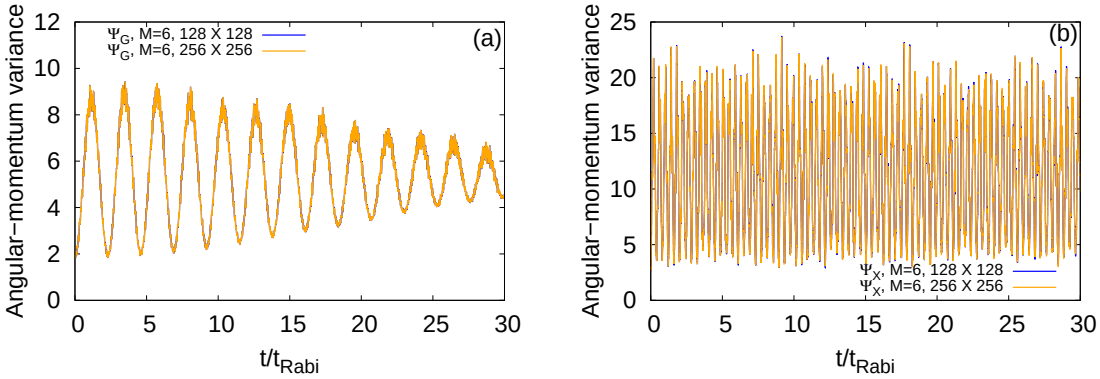

FIG. S14. Convergence of the time-dependent variance per particle of the z- component of the angular-momentum operator, $\frac{1}{N}\Delta^2_{\hat{L}_Z}(t)$, with the he number of grid points. Initial states are (a) Ψ_G ($\omega_n = 0.19$) and (b) Ψ_X ($\omega_n = 0.18$) in transversely-asymmetric 2D double-well potential. The bosonic clouds consist of $N = 10$ bosons with the interaction parameter $\Lambda = 0.01\pi$. The convergence is demonstrated with 128×128 and 256×256 grid points. We show here dimensionless quantities. Color codes are explained in each panel.

[1] Streltsov, A. I., Alon, O. E. & Cederbaum, L. S. Role of excited states in the splitting of a trapped interacting Bose-Einstein condensate by a time-dependent barrier. Phys. Rev. Lett. **99**, 030402 (2007).

[2] Alon, O. E., Streltsov, A. I. & Cederbaum, L. S. Multiconfigurational time-dependent Hartree method for bosons: many-body dynamics of bosonic systems. Phys. Rev. A **77**, 033613 (2008).

[3] Lode, A. U. J., Lévêque, C., Madsen, L. B., Streltsov, A. I. & Alon, O. E. Colloquium: Multiconfigurational time-dependent Hartree approaches for indistinguishable particles. Rev. Mod. Phys. **92**, 011001 (2020).

[4] Streltsov, A. I. & Streltsova, O. I. MCTDHB-Lab, Version 1. 5. 2015. Available online: (http://mctdhb-lab.com).

[5] Streltsov, A. I., Cederbaum, L. S., Alon, O. E., Sakmann, K., Lode, A. U. J., Grond, J., Streltsova, O. I., Klaiman, S. & Beinke, R. The Multiconfigurational Time-Dependent Hartree for Bosons Package, Version 3.x. Available online: http://mctdhb.org.

[6] Klaiman, S., & Alon, O. E. Variance as a sensitive probe of correlations. Phys. Rev. A **91**, 063613 (2015).

[7] Klaiman, S., Streltsov, A. I. & Alon, O. E. Uncertainty product of an out-of-equilibrium many-particle system. Phys. Rev. A **93**, 023605 (2016).

[8] Alon, O. E. Analysis of a Trapped Bose-Einstein Condensate in Terms of Position, Momentum, and Angular-Momentum Variance. Symmetry **11**, 1344 (2019).

[9] Sakmann, K. & Schmiedmayer, J. Conserving symmetries in Bose-Einstein condensate dynamics requires many-body theory. arXiv:1802.03746v2.

[10] Bhowmik, A., Haldar, S. K. & Alon, O. E. Impact of the transverse direction on the many-body tunneling dynamics in a two-dimensional bosonic Josephson junction. Sci Rep **10**, 21476 (2020).